

SANTA BARBARA CLUSTER COMPARISON TEST WITH DISPH

TAKAYUKI R. SAITOH¹ & JUNICHIRO MAKINO^{1,2,3}

Draft version August 13, 2018

ABSTRACT

The Santa Barbara cluster comparison project (Frenk et al. 1999) revealed that there is a systematic difference between entropy profiles of clusters of galaxies obtained by Eulerian mesh and Lagrangian smoothed particle hydrodynamics (SPH) codes: Mesh codes gave a core with a constant entropy whereas SPH codes did not. One possible reason for this difference is that mesh codes are not Galilean invariant. Another possible reason is the problem of the SPH method, which might give too much “protection” to cold clumps because of the unphysical surface tension induced at contact discontinuities. In this paper, we apply the density independent formulation of SPH (DISPH), which can handle contact discontinuities accurately, to simulations of a cluster of galaxies, and compare the results with those with the standard SPH. We obtained the entropy core when we adopt DISPH. The size of the core is, however, significantly smaller than those obtained with mesh simulations, and is comparable to those obtained with quasi-Lagrangian schemes such as “moving mesh” and “mesh free” schemes. We conclude that both the standard SPH without artificial conductivity and Eulerian mesh codes have serious problems even such an idealized simulation, while DISPH, SPH with artificial conductivity, and quasi-Lagrangian schemes have sufficient capability to deal with it.

Subject headings: galaxies:clusters:general—galaxies:evolution—methods:numerical

1. INTRODUCTION

Frenk et al. (1999) conducted a comparison project of numerical simulations of the formation of a massive cluster of galaxies in a cold dark matter (CDM) universe in which the results of twelve independent simulation codes were compared. Both Eulerian mesh codes and Lagrangian smoothed particle hydrodynamics (hereafter SPH; Lucy 1977; Gingold & Monaghan 1977) codes were used in this comparison project. In this project, they took into account only gravity and hydrodynamics so that the comparison was simplified. This project is known as the “Santa Barbara cluster comparison project”.

Although most of global properties reasonably converged, there was a systematic difference in entropy profiles of the clusters in simulations with different methods. The results of the Eulerian mesh codes showed the central core in entropy profiles, whereas those of SPH codes did not (see figure 18 in their paper). Later studies confirmed this tendency (e.g., Kravtsov et al. 2002; Ascasibar et al. 2003; Springel 2005; Voit et al. 2005; Mitchell et al. 2009; Vazza 2011; Almgren et al. 2013). Frenk et al. (1999) interpreted that this difference might reflect the difference in the treatment of shocks of SPH and mesh codes.

Agertz et al. (2007) pointed out that there are “fundamental differences” between Eulerian mesh and Lagrangian SPH codes (see also Ritchie & Thomas 2001; Okamoto et al. 2003). This difference is originated from the fact that the standard formulation of SPH (hereafter

SSPH⁴) has difficulties when dealing with contact discontinuities. Since SSPH requires the differentiability of the density field, the density around a contact discontinuity has a large error. In particular, the density of particles in the low-density side of the contact discontinuity is overestimated by a large factor. This error propagates to the pressure evaluation, resulting in the *unphysical surface tension* and the suppression of fluid instabilities (See figure 1 in Saitoh & Makino 2013).

We can solve this problem by using the volume element which does not depend on the density (Ritchie & Thomas 2001; Read et al. 2010; Saitoh & Makino 2013; Hosono et al. 2013; Hopkins 2013; Rosswog 2015), by introducing extra dissipation terms (Price 2008; Read & Hayfield 2012; Kawata et al. 2013), by using the integration form to evaluate the derivatives of physical quantities (García-Senz et al. 2012; Rosswog 2015), by employing the non-standard equation of motion which breaks Newton’s third law (Abel 2011), and by adopting the Godunov SPH (Inutsuka 2002) where physical quantities are smoothed twice (Cha et al. 2010). Yamamoto et al. (2015) used a diffusive quantity, y , instead of the mass and mass density, to formulate the SPH approximation. Each particle has the Y , and from that its density is calculated using the usual formula to calculate mass density from mass of particles in SPH.

Since all of the SPH codes used in the Santa Barbara cluster comparison project were based on SSPH, the cuspy entropy profile obtained with SPH codes might be, at least partly, the artifact caused by the unphysical surface tension. In the hierarchical structure formation scenario, a cluster of galaxies grows through mergers of a

saitoh@elsi.jp

¹ Earth-Life Science Institute, Tokyo Institute of Technology, 2–12–1, Ookayama, Meguro, Tokyo, 152-8551, Japan

² Department of Planetology, Graduate School of Science / Faculty of Science, Kobe University 1-1, Rokkodai-cho, Nada-ku, Kobe, Hyogo, Japan, 657-8501

³ RIKEN Advanced Institute for Computational Science, Minatojima-minamimachi, Chuo-ku, Kobe, Hyogo, 650-0047, Japan

⁴ Following Saitoh & Makino (2013), we call “SSPH” the SPH formulation using m/ρ , where m and ρ are the mass and density of a particle, as the discrete volume element for the discretization of the equations.

number of small building blocks which contain cold, low-entropy gas. The unphysical surface tension of SSPH tends to protect cold gas clumps in the building blocks against the fluid instabilities and the ram-pressure stripping, as demonstrated by the “blob test” of Agertz et al. (2007). As a result, cold clumps might reach the center of the cluster due to the dynamical friction with keeping their low entropy state, resulting in a cuspy entropy profile of the cluster.

Some of techniques described above have been applied to the cluster formation simulations in order to investigate their effect on the central entropy structure. Wadsley et al. (2008) added a diffusion term to the energy equation which mimics the turbulence mixing⁵ and performed the Santa Barbara cluster simulations. They found that the entropy core could be formed, but the size and depth of the entropy core depended strongly on the diffusion coefficient and numerical resolutions (see their figures 12 and 13). Power et al. (2014) carried out a set of comparison tests of the cluster formation in a Λ CDM universe with SPH and an adaptive mesh refinement (AMR) codes, focusing on the formation of the entropy core. In their comparison tests, they used not only SSPH but also their new SPH, SPHS (Read & Hayfield 2012) which avoids multivalued of physical quantities by artificial diffusion terms with a higher order dissipation switch and increases the force accuracy by adopting a higher order kernel with a large number of neighbor particles. In SPHS runs, the entropy core was formed in the cluster center and its size was consistent to that obtained by an AMR code, *Ramses* (Teyssier 2002). This good agreement is achieved when the maximum dissipation parameter $\alpha_{\max} \geq 1$ (see their figure 6). On the other hand, in the case with $\alpha_{\max} = 0.1$, the entropy profile has a core, but it is smaller and the core entropy is lower than those with converged values. In the case with $\alpha_{\max} = 0$, it is close to that found with SSPH. Recently, Sembolini et al. (2016) reported a new comparison test of a numerical cluster in a Λ CDM universe. They showed that SPH codes with the artificial conductivity (hereafter AC) term and SPHS give entropy profiles which are close to those given by AMRs (i.e., cored profiles), although they did not provide the results of the parameter tests.

The agreement with the results of AMR calculations does not guarantee the validity of the results, since Eulerian schemes have their own limitations. An obvious one comes from its Eulerian nature. In order to integrate the motion and internal energy of fast-moving cold gas clump, very high accuracy is required. The internal energy of a gas clump can be many orders of magnitudes smaller than its kinetic energy in the reference frame of the mesh. Numerical error comes from the kinetic energy, but it affects the internal energy of the clump. Consider the case that a molecular cloud moves in a galaxy following the galactic potential. The typical temperature of the cloud is ~ 10 K while the virial temperature which corresponds to the typical kinematic energy is $\sim 10^6$ K for a galaxy of the Milky Way size. The energy difference between the thermal and kinetic energies of the cloud be-

comes about five orders of magnitude. Very high accuracy is, thus, required to keep the structure of the clump, and this requirement in turn results in the requirement of high spacial resolution and small time step. Otherwise, a large error is induced by the loss of significant digits and/or negative pressure. A remedy for this problem is the dual energy formulation (Bryan et al. 1995). In this formulation, both total (E_{tot}) and internal (E_{th}) energies are solved independently. Then, either E_{th} or $E_{\text{tot}} - E_{\text{kin}}$, where E_{kin} is the kinetic energy, is used to evaluate pressure, depending on the fraction of the thermal energy. For the high Mach number fluid, e.g., $(E_{\text{tot}} - E_{\text{kin}})/E_{\text{tot}} < 10^{-3}$, E_{th} is adopted to evaluate pressure. Otherwise, since $E_{\text{tot}} \sim E_{\text{kin}}$, the loss of significant digits occurs.

Another difficulty is that the Eulerian formulation is not the Galilean invariant, which leads to the numerical diffusion. An example of this problem can be seen in figure 14 of Tasker et al. (2008). In Eulerian codes, an initially hydrostatic cluster decays after 1 Gyr evolution, in particular in *Enzo* (Bryan & Norman 1997) with *Zeus* (Stone & Norman 1992) and *FLASH* (Fryxell et al. 2000), when a translational velocity was added. In principle, by going to higher spatial resolution, we can reduce the rate of decay by reducing the effect of the numerical dissipation (Robertson et al. 2010). Nevertheless, compared to Lagrangian codes with the same effective accuracy, the computational cost would be much higher. The other way is to adopt higher spatial order schemes, such as essentially non-oscillatory polynomial interpolation (ENO; Harten et al. 1987), weighted ENO (WENO; Liu et al. 1994), and constrained interpolation profile (CIP; Yabe & Aoki 1991) schemes. However, these schemes are computationally expensive and it is difficult to combine high-order schemes with AMR in a consistent way. The latter is serious because joint interfaces of finer and coarse meshes lose their accuracy (Li 2010) and thus careful treatment is necessary.

Recently, novel numerical schemes have been developed and used in the field of numerical astrophysics. Springel (2010) developed a moving mesh scheme which is free from the above problem of the Eulerian mesh codes. In Springel (2010), he carried out simulations of the Santa Barbara cluster with “*AREPO*”, an implementation of his moving mesh scheme, and reported that the entropy core was formed. The size of the core is smaller than those obtained by AMR simulations and the entropy at the core is lower than those obtained by AMR simulations. Hopkins (2015) developed a new code “*GIZMO*” which implemented a meshless method and found that in cluster simulations with *GIZMO* entropy cores similar to those of *AREPO* is formed. These results are quite encouraging. However these two codes use similar approaches, such as quasi-Lagrangian nature using Riemann solvers. Further tests with different schemes are important.

In this paper, we report the results of Santa Barbara cluster simulations obtained with the density independent formulation of SPH (*DISPH*) (Saitoh & Makino 2013). Since *DISPH* is free from the unphysical surface tension, we can expect that it gives better results compared to SSPH. In addition, since *DISPH* do not introduce artificial dissipations, we can expect that the result is not affected by free parameters.

⁵ The additional term they used is very close to the artificial conductivity term proposed by Price (2008). Formally, the difference between two methods can be reduced the difference in the adopted forms of the signal velocity (Price 2012).

The structure of this paper is as follows. In §2 we give a brief review of the formulation of SSPH and DISPH and their advantages and disadvantages. We then describe the initial condition and our numerical methods in §3. The comparison is carried out in §4 and discussion is given in §5.

2. DIFFERENCES BETWEEN SSPH AND DISPH

In the SPH method, all physical quantities are evaluated using the kernel approximation over the field discretized by particles. The kernel approximation for a physical quantity f is given by

$$f(\mathbf{x}) = \int_{-\infty}^{\infty} f(\mathbf{x}')W(\mathbf{x}' - \mathbf{x}, h)d\mathbf{x}', \quad (1)$$

where \mathbf{x} and \mathbf{x}' are position vectors, W is a function with a compact support called the kernel function, and h is the kernel size. We approximate this spatial integration by the summation over particles expressed as

$$f_i = \sum_j f_j W(\mathbf{x}_j - \mathbf{x}_i, h_i) V_j, \quad (2)$$

where f_i and f_j are the values of f at the positions of particles i and j , respectively, and V_j is the volume element associated with particle j . In SSPH, we use

$$V_j = \frac{m_j}{\rho_j}, \quad (3)$$

where m_j and ρ_j are the mass and density of particle j , respectively. From Eqs. (2) and (3), by substituting ρ into f , we have

$$\rho_i = \sum_j m_j W(\mathbf{x}_j - \mathbf{x}_i, h_i). \quad (4)$$

Note that Eq. (4) gives the *smoothed* estimate of the density field. Thus, the density near a contact discontinuity suffers a very large error. Consider the case that we evaluate the density around a contact discontinuity using Eq (4). The density of a particle at the low-density side is over-estimated, while that of a particle at the high-density side is under-estimated. The absolute amount of the error is similar at the both sides. The relative error is much larger at the low-density side, simply because the true density is smaller. This large overestimate of the density results in equally large overestimate of the pressure for low-density particles near the contact discontinuity, which then causes a strong repulsive force. This repulsive force works as an unphysical surface tension (e.g., Ritchie & Thomas 2001; Okamoto et al. 2003; Agertz et al. 2007; Read et al. 2010). If the distribution of the internal energy is sufficiently smooth, this unphysical surface tension does not show up even with the smoothed density. The AC term introduced by Price (2008) automatically reduces the pressure jump by spreading the internal energy.⁶ A switch is always used to avoid unnecessary diffusion.

In DISPH, unlike SSPH, the pressure (or its arbitrary function) is used to evaluate the volume element

⁶ Although AC can eliminate the unphysical surface tension, we consider that it is not always an adequate solution. For instance, AC has difficulty dealing with a fluid system with different chemical compositions. See appendix A.

(Saitoh & Makino 2013; Hopkins 2013; Hosono et al. 2013; Rosswog 2015). The pressure field is smooth everywhere, except at the shock front. In SPH, the shock is handled by the artificial viscosity (hereafter AV) which smooths the velocity field and prevents multivalued. As a by-product, we have a smoothed pressure distribution in SPH simulations, even at the shock front. Therefore, we can expect that the problem of SSPH at the contact discontinuity is solved if we use a volume element based on the pressure. This is the basic idea of DISPH. The simplest form of the fundamental equation used in DISPH can be obtained by using the volume element $V_j = U_j/q_j$, where q_j and U_j are the energy density and the internal energy of particle j , respectively. Substituting q into f in Eq. (2) and using the energy density based volume element, we have

$$q_i = \sum_j U_j W(\mathbf{x}_j - \mathbf{x}_i, h_i). \quad (5)$$

Since the pressure is smooth at contact discontinuities and even at the shock front, we can obtain smoothed values without large errors. Note that, if one uses DISPH for a non-ideal gas, one needs to use pressure directly instead of the energy density (Hosono et al. 2013), because it is no longer smooth. We note that this formulation itself does not introduce any dissipation.

In DISPH, as a trade-off for using of the smoothed pressure for the formulation, the density distribution has a jump at a contact discontinuity if the internal energy distribution there is not smooth (see figure 2 in Saitoh & Makino 2013). While this jump does not affect the motion of particles, it is necessary to be aware of this “unphysical” density jump when one uses this density to evaluate physical quantities, such as radiative cooling. As is noted by Saitoh & Makino (2013) and Hopkins (2013), the simplest solution is to use the smoothed density.

In the same manner as SSPH, DISPH can conserve the total energy, linear and angular momentum. If we use a variation principle for the derivation of SPH equations (Springel & Hernquist 2002), we can obtain a set of conservative SPH equations (Hopkins 2013). The equations in this derivation have the so-called “grad- h ” term. Moreover, if we carefully constructs energy and momentum equations, we can obtain another set of the conservative equations which do not involve the grad- h term (see section 5.6 in Saitoh & Makino 2013). Here we adopt DISPH with the grad- h term, which is more robust under the strong shock. In appendix B, we show the result of the three-dimensional collapse test (Evrard 1988). The relative energy error from the beginning and the end of the simulation is $\sim 0.2\%$, which is comparable to the previous studies (e.g., Springel et al. 2001; Springel 2005).

3. METHOD

3.1. Initial condition

The initial condition we used here is basically the same as that used in Heitmann et al. (2005). The volume of their initial condition is 64^3 Mpc^3 in the comoving space and the initial redshift is $z = 63$. The 3σ overdensity is imposed at the center of the volume so that a massive cluster will be formed at the center. There are two set of initial conditions with different resolutions: 128^3

and 256^3 particles. The cosmology is the standard CDM and the Hubble parameter is $H_0 = 100 h \text{ km s}^{-1} \text{ Mpc}^{-1}$ where $h = 0.5$.

We integrated the formation and evolution of the Santa Barbara cluster with a vacuum boundary condition in the physical space. We cut the central spherical volume with the radius of 32 Mpc in the comoving space and remapped it to the physical space at $z = 63$. Then, we imposed the Hubble flow corresponding to the initial redshift. Following Frenk et al. (1999), we assumed $\Omega_{\text{DM}} = 0.9$ and $\Omega_{\text{baryon}} = 0.1$. Since the original initial conditions of Heitmann et al. (2005) are for DM only simulations, we divided each particle into two particles which have the same position and velocity of the original particle but have different masses, i.e., that one has 90% and the other has 10% of the original particle mass, for simulations involving both DM and gas.

The number of particles, the mass of particles and the spatial resolutions (softening lengths for DM and baryon: ϵ_{DM} and ϵ_{baryon}) are summarized in table 1. For both of low- and high-resolution models, we performed two runs, one with the standard SPH, and the other with DISPH. We carried out five high-resolution SSPH runs involving AC. These five runs adopted different values for the maximum dissipation parameter. In addition, two extra models which combine the low mass and the high spatial resolutions (Mixed 1) and the high mass and the low spatial resolutions (Mixed 2) are adopted in order to investigate the effect of the resolutions further. We also carried out two runs with SSPH and DISPH for each model. Thus, in total we performed thirteen runs.

3.2. Numerical techniques

We used a parallel N -body/SPH code ASURA (Saitoh et al. 2008, 2009) for this experiment. The gravitational interactions between particles were calculated by the tree method (Barnes & Hut 1986). The tree with GRAPE method (Makino 1991b) was used. The parallelization method of the gravity calculation was that proposed by Makino (2004). We adopted the symmetrized Plummer potential and its multipole expansion (Saitoh & Makino 2012) so that we can calculate the gravitational interactions between particles with different values of softening lengths by a single tree. The opening angles for the ordinary three dimensions and softening lengths were set to 0.5 following Saitoh & Makino (2012). The phantom-GRAPE library was used for the calculation of particle-particle interactions in order to accelerate the calculation (Tanikawa et al. 2013).

The equation of state of the ideal gas with the specific heat ratio $\gamma = 5/3$ was used. In order to handle shocks, the AV term proposed by Monaghan (1997) was used. In addition to this, we used an AV switch proposed by Morris & Monaghan (1997) in which the value of the AV parameter, α , changes in the range of 0.1 – 1. Following Rosswog (2009), a modification which accelerates the increase of α at lower α regime and slows it at higher α regime was also used. The Balsara limiter (Balsara 1995) was adopted in order to reduce the shear viscosity. We employed the Wendland C4 kernel which is free from the paring instability (Wendland 1995; Dehnen & Aly 2012). The number of neighbor particles was kept within 128 ± 8 . This higher order kernel with a larger number of neighbor particles can reduce the so-called E0 error (Read et al.

2010).

The time integration was carried out by a second order scheme (see appendix §B for details). The individual and hierarchical time-step methods were used (McMillan 1986; Makino 1991a). For SPH particles, the time-step limiter, which enforces the time-step difference among neighboring particles to be small enough to follow strong shocks, was used (Saitoh & Makino 2009). The FAST scheme, which allows each particle to have different time-steps for gravitational and hydrodynamical interactions and integrates these two interactions independently, was also adopted (Saitoh & Makino 2010). When we used the FAST scheme, the computational time (wall-clock time) became half of what it was without FAST (we used 128 CPU cores of Cray XC30 in this comparison). This gain is almost the same as that reported in Saitoh & Makino (2010), although simulation setups in both runs were completely different.

3.3. Detection of the Santa Barbara Cluster

Following previous studies (Frenk et al. 1999; Heitmann et al. 2005), we define a dense region which is formed at the center of the simulation volume and with the mean density is 200 times higher than the background density as the ‘‘Santa Barbara cluster’’. We express the radius where the mean density becomes 200 times of the background density as R_{200} and call it the virial radius.

The procedure to find the center and size of the Santa Barbara cluster is as follows. First, we find a particle of which total energy is the lowest and adopt it as the center of the cluster of galaxies. Then, we sort all of particles based on the distance from the center of the cluster in ascending order. We calculate the mean density from the center to the outer part following the particle order, and we halt this operation when the mean density becomes less than 200 times of the background density. We regard the distance from the center to the particle position where we halt this operation as the virial radius. This simple strategy works well for the Santa Barbara test in which a single massive cluster is formed near the center of the simulation volume.

3.4. Definitions of the Density Center and the Core Radius

In order to draw radial profiles, we use a density weighted center instead of the halo center since the peak of the baryon distribution does not always coincide with the position of particle with the lowest total energy. We use the following definition as the density weighted center (von Hoerner 1960, 1963):

$$\mathbf{x}_c = \frac{\sum_j \rho_j \mathbf{x}_j}{\sum_j \rho_j}, \quad (6)$$

where we only take care of the gas particles in the virial radius. For this density ρ_j , we just used the SSPH-estimated density. The kernel function and the number of neighbor particles are the same as those described in §3.2.

4. RESULTS

In this section, we compare the properties of the Santa Barbara cluster obtained by simulations with SSPH and

TABLE 1
NUMBER AND MASS OF PARTICLES AND SPATIAL RESOLUTIONS.

Run type	Number	DM mass	Baryon mass	ϵ_{DM}	ϵ_{Baryon}
Low resolution	2202482 (1101241 \times 2)	$7.8 \times 10^9 M_{\odot}$	$8.8 \times 10^8 M_{\odot}$	20 kpc	10 kpc
High resolution	17619230 (8809615 \times 2)	$9.6 \times 10^8 M_{\odot}$	$1.1 \times 10^8 M_{\odot}$	10 kpc	5 kpc
Mixed resolution 1	17619230 (8809615 \times 2)	$9.6 \times 10^8 M_{\odot}$	$1.1 \times 10^8 M_{\odot}$	20 kpc	10 kpc
Mixed resolution 2	2202482 (1101241 \times 2)	$7.8 \times 10^9 M_{\odot}$	$8.8 \times 10^8 M_{\odot}$	10 kpc	5 kpc

DISPH, and then investigate the origin of the difference in the entropy profile. We first describe the global properties of the Santa Barbara cluster in §4.1. The density, temperature and entropy distributions in the clusters obtained by simulations with SSPH and DISPH at $z = 0$ are compared in §4.2. In §4.3, we compare radial profiles. We investigate how the central entropy core/cusp formed in §4.4. In §4.5, we investigate the contribution of the AC term for the cluster entropy profile.

In order to avoid confusion, we use the label “SPH” to indicate the results of SSPH on figures and “DISPH” for the results of DISPH.

4.1. Global Properties of the Santa Barbara Cluster at $z = 0$

The average of virial radii of the Santa Barbara clusters of the four runs (the high- and low-resolution runs with SSPH and DISPH) is $R_{200} \sim 2.9$ Mpc. This radius is somewhat larger than those obtained in previous studies (Frenk et al. 1999; Heitmann et al. 2005). The total mass within R_{200} is $\sim 1.4 \times 10^{15} M_{\odot}$ which is 16% larger than those obtained by Heitmann et al. (2005). These differences are probably due to the difference in the treatment of the boundary condition. We used the open boundary condition, while all runs in Heitmann et al. (2005) adopted the periodic boundary condition. Since the radius of the initially imposed overdensity region is 10 Mpc, the cut-off radius of 32 Mpc would be insufficient to remove boundary effects. Nonetheless, as we see later, the central region of the cluster does not seem to be affected by the boundary condition. In the following, we call the Santa Barbara cluster just “cluster”, for brevity.

We found that the clusters obtained by DISPH contain more gas than those obtained by SSPH. The gas fractions of the cluster with DISPH are 0.097 – 0.098 which are close to the results of high resolution mesh codes in Frenk et al. (1999) and also the cosmic averaged value of 0.1 for this model. On the other hand, those of SSPH are 0.093 – 0.094 which are close to those of SSPH runs in Frenk et al. (1999), ~ 0.09 .

4.2. Snapshots of the Santa Barbara Cluster at $z = 0$

Figure 1 shows the gas density maps of the four runs within R_{200} at $z = 0$. These density maps are not very different. However, when we inspect these maps carefully, we find several differences. First, we can see that the central densities in runs with SSPH are higher than those with DISPH. The density of the innermost regions of the clusters with SSPH is one order of magnitude higher than that with DISPH. Second, for both of SSPH and DISPH runs, the central density of the cluster is higher for runs with high mass resolution (large number of particles).

Figure 2 shows the temperature distribution within the cluster of four runs. We can see that the clusters of SSPH

runs contain more small-scale substructures compared to those of DISPH runs.

Figure 3 shows the entropy distributions; the definition of the entropy we adopted in this paper is

$$s \equiv \ln(T/\rho^{2/3}), \quad (7)$$

where T and ρ are the temperature in the unit of Kelvin and the density in the unit of $M_{\odot} \text{ Mpc}^{-3}$, respectively, and this definition is the same as that used in Frenk et al. (1999). It is obvious that the values of the central entropy in SSPH runs are much lower than those in DISPH runs. The clusters in DISPH runs have no or a little amount of gas with entropy below -4 , while the clusters in SSPH runs have significant amounts of such gas at the center. It is also clear that the entropy distributions of the cluster in DISPH runs are smoother than those of clusters in SSPH runs. In other words, the entropy distribution indicates that the gas in the clusters of SSPH runs is not well mixed.

4.3. Radial Profiles of the Santa Barbara Cluster at $z = 0$

Figure 4 shows the radial profiles of the cluster at $z = 0$. In this figure, we used two high-resolution results. In this plots, “SB” denotes the averaged profiles in Frenk et al. (1999), “AREPO” is the result of a moving mesh code AREPO by Springel (2010)⁷, and “Nyx” denotes the result of an AMR code Nyx by Almgren et al. (2013).⁸ We note that these data were taken from figures in their papers: figure 18 in Frenk et al. (1999) for SB, figure 45 in Springel (2010) for AREPO (we adopt the result labeled 128³), and figure 7 in Almgren et al. (2013) for Nyx. We also note that the entropy profile with GIZMO reported by Hopkins (2015) is comparable to that with AREPO.

The density profiles of DM (the top-left panel of figure 4) of all four runs agree very well. The central density of gas of the SSPH run is significantly higher than those of the other three runs. Here, “SB”, “AREPO” and our DISPH results seem to agree well. Note, however, that the “SB” plot is the average of 7 SPH and 5 mesh-based

⁷ We note that the plot data of “AREPO” is based on the run with the “entropy-energy formalism”, where the value of the entropy is completely conserved in all cells whose Mach numbers are less than 1.1. As expected, with this formalism the entropy generation is slightly suppressed (Sijacki et al. 2012). On the other hand, Hopkins (2015) pointed out that spurious heating from Riemann solver errors affects an entropy profile when this formalism turned off. Hence, we adopt the original data shown in Springel (2010).

⁸ Nyx is a N -body/gas dynamics code designed for large scale cosmological simulations. In this code, the fluid evolution is solved by a finite volume method with a block structured AMR. The dual energy formulation is used. The Riemann solver is used for the evaluation of fluxes. According to these features, Nyx is one of good representatives of the state-of-the-art AMR codes. The entropy profile of the Santa Barbara cluster with Nyx is almost identical to those with Enzo (Bryan et al. 1995) and ART (Kravtsov et al. 2002).

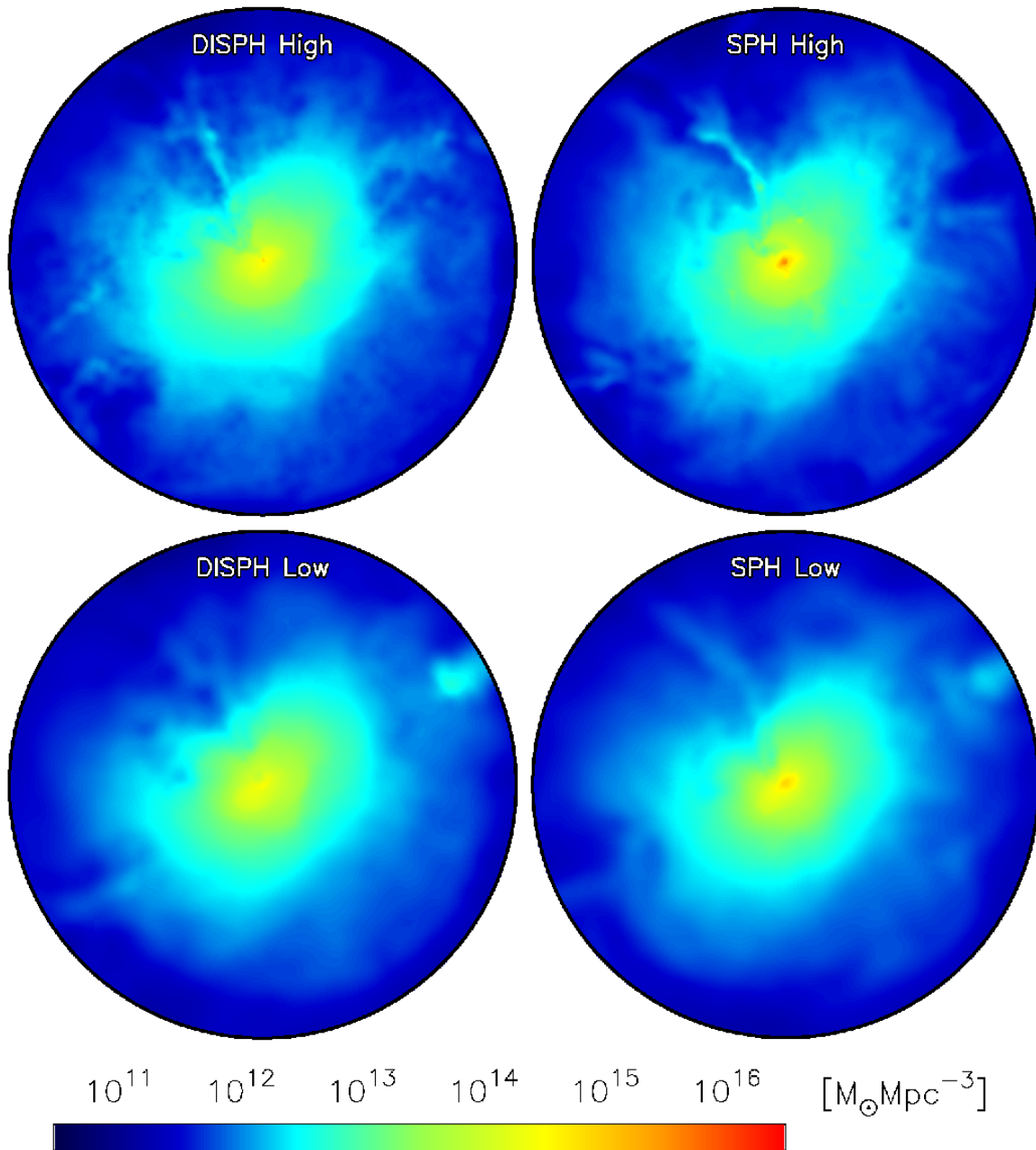


FIG. 1.— Density maps of four runs at $z = 0$. The center of the cluster is adopted as the center of the coordinates. The radius of the plot region in each density map is corresponding to the virial radius. In the virial radius, we paved meshes whose sizes are $\sim 60 \text{ kpc}^2$ and then evaluated the density of each mesh center using Eq. 4 where the neighbor number is 128 ± 8 . We did not apply any smoothing filter for these maps.

scheme runs, and SPH models in Frenk et al. (1999) gave the result similar to our SSPH run, while the mesh runs gave a central density even lower than AREPO/DISPH results. Thus, the agreement between our DISPH result and the AREPO result is rather good, whereas all SSPH runs gave high central densities and AMR runs, lower density.

From the temperature profile (the left-bottom panel of figure 4) and density profile (the top-right panel) of the gas component, we can see that the standard SPH gives a central cusp with the temperature decreasing inward, while AREPO and DISPH give constant-density, constant-temperature cores. Mesh runs in Frenk et al.

(1999) also gave constant-density cores, but their cores are systematically larger than those obtained by AREPO and our DISPH. The averaged “SB” profile of the temperature shows a sign of central decrease, since it is the average of SPH (decreasing) and mesh (increasing) profiles. We can see the same tendency in the entropy profile (the bottom-right panel).

In figure 5, we plot the entropy profiles of our low-resolution runs, as well as those of our high-resolution runs and three results from the literature (“SB”, “AREPO” and “Nyx”). We can see that for DISPH runs, the difference in resolution does not make much difference in the entropy profile; the entropy pro-

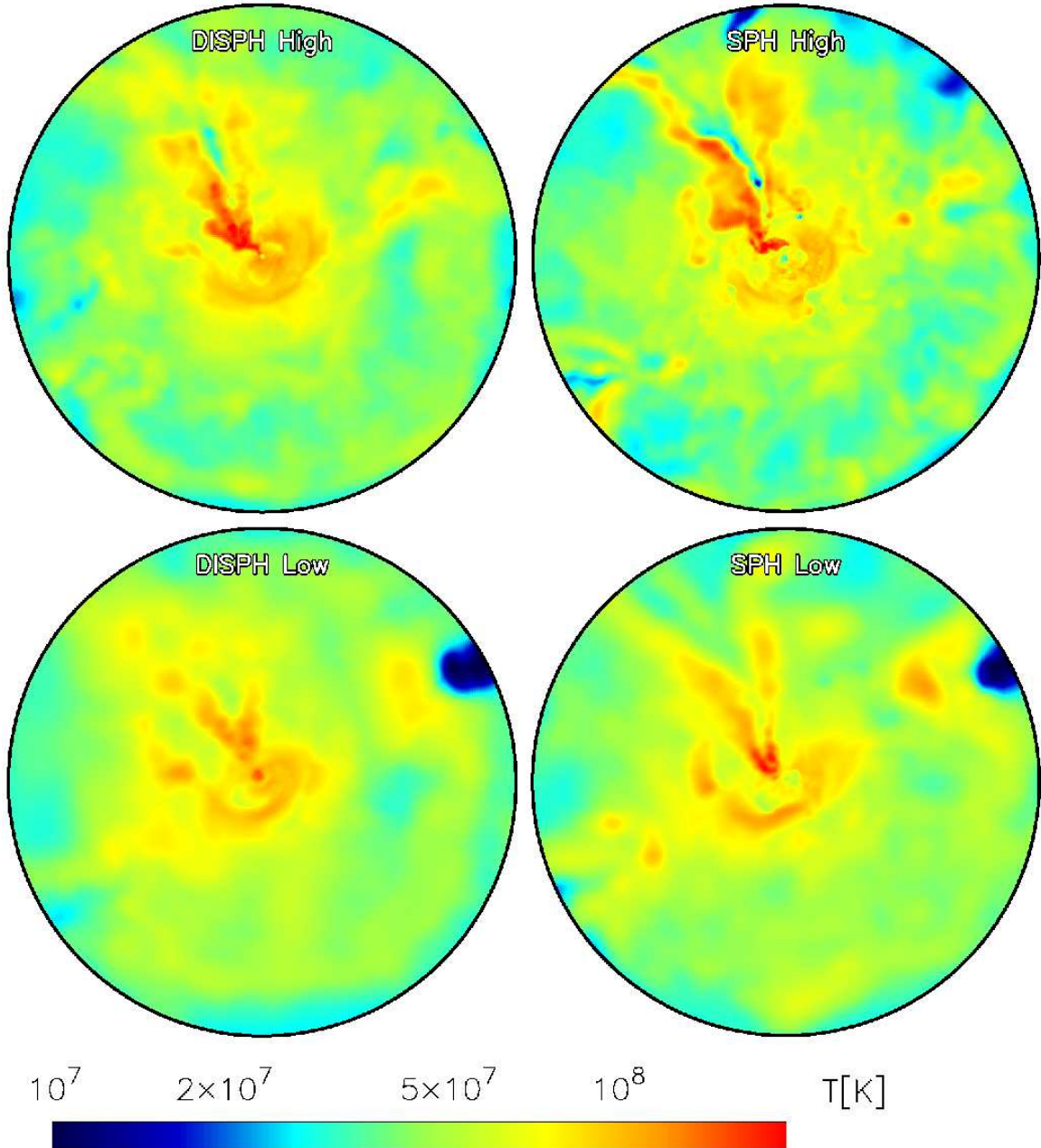


FIG. 2.— The same as figure 1 but for temperature.

files with DISPH are consistent with that obtained by a moving mesh code AREPO. On the other hand, our low-resolution SSPH run gave a central entropy significantly higher than that of our high-resolution SSPH run. Our low-resolution SSPH result is similar to those of the SSPH simulations in Frenk et al. (1999) and Springel (2010). Thus, it is clear that the “core” in these previous SSPH results is due to the limitations in the numerical resolution.

From this figure, we find that the central entropy in the high-resolution DISPH run is slightly higher than that in the low-resolution DISPH run, although we saw the opposite sense from the entropy maps (figure 3). This is because there is an offset of ~ 50 kpc between the position of the entropy minimum and the plot center (the density weighted center) in the high-resolution DISPH

run, and it makes the rather flatter central entropy profile. Thus, there is no discrepancy.

In order to assess which parameters, i.e., mass and spatial resolutions, are more crucial to the final entropy profile of the cluster, we carried out two extra models with DISPH and SSPH which mix resolutions; (1) with the high mass/low spatial resolutions (“Mixed resolution 1”) and (2) with the low mass/high spatial resolutions (“Mixed resolution 2”). As shown in figure 6, the former run reproduced the entropy profile of the high-resolution SSPH run, while the latter run did that of the low-resolution SSPH run. A slight difference is found only in the very central region ($R_d < 20$ kpc). Hence, in the SSPH runs, the central structure of the entropy profile is sensitive to the small scale power of the initial density fluctuations. There is no significant influence on the

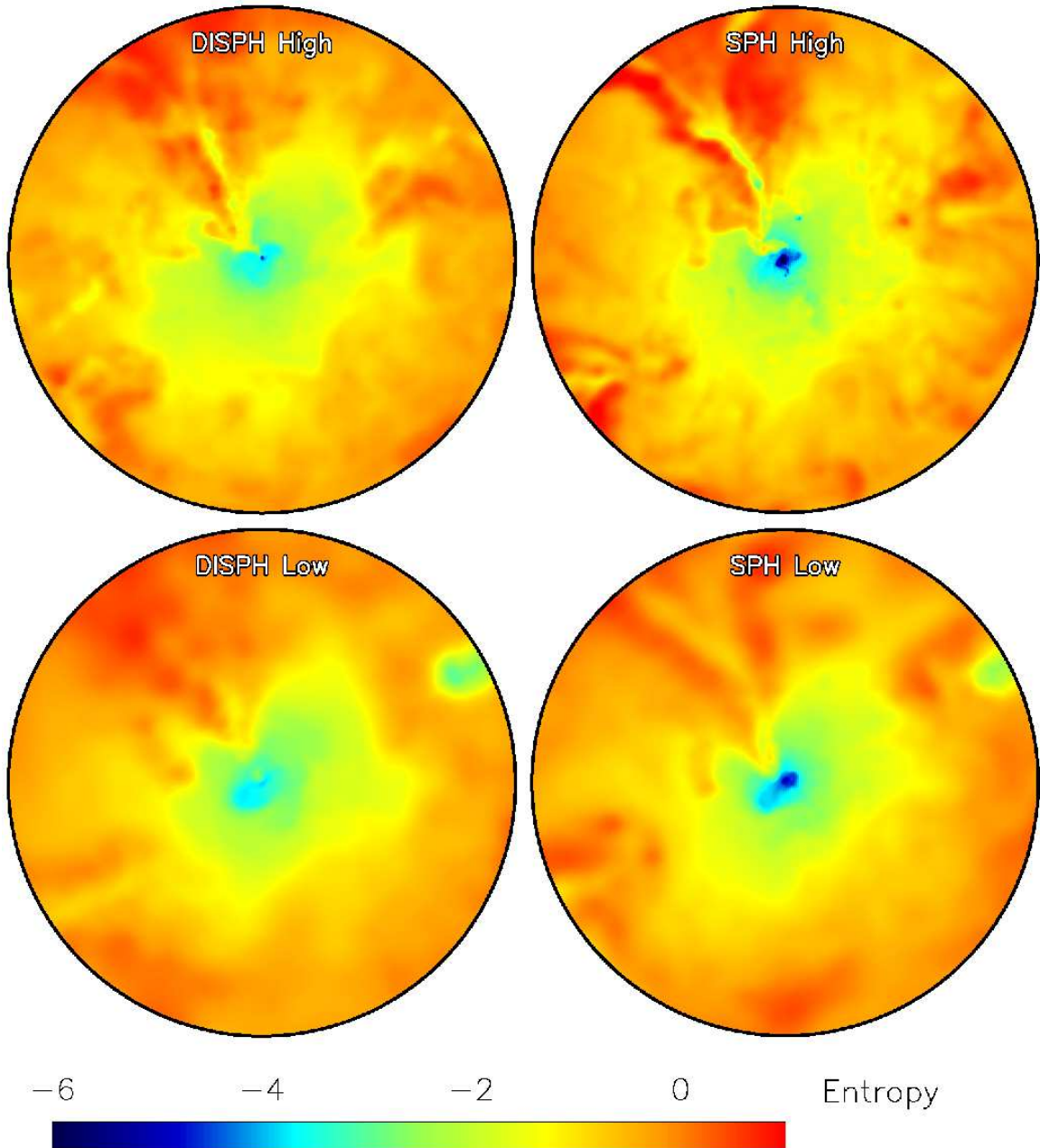


FIG. 3.— The same as figure 1 but for entropy.

results with DISPH.

The good agreement between results with DISPH, AREPO, and GIZMO is quite encouraging. However, the analysis so far is only limited at the date of $z = 0$. In the next subsection, we compare the results obtained by DISPH and SSPH methods deeply, by focusing on the formation process of the cluster.

4.4. Entropy Core/Cusp Formation

The cluster grew rapidly while $z > 1$, and then experienced a major merger around $z \simeq 0.7$, and evolved mildly until $z = 0$. We follow these typical phases of evolution to understand how and when the entropy core and cusp are established.

Figure 7 shows the radial entropy and density profiles for the high-resolution DISPH and SSPH runs. We here

plot them for three epochs, before the major merger ($z = 1$), after the major merger ($z = 0.5$), and at the end of the simulation ($z = 0$).

For the run with DISPH, at $z = 1$, the entropy profile has a relatively small core. Then, the core entropy and core size increase and these quantities are kept unchanged until $z = 0$. The entropy profile at $z = 0.5$ is comparable to that at $z = 0$; the last major merger event triggers this core entropy increase (see below). The entropy of the intermediate region of $40 \text{ kpc} \leq R_d \leq 1 \text{ Mpc}$ slightly increased during $0 < z < 0.5$. The evolution of the density profile is similar, but in the opposite direction. The core density decreases by almost a factor of three from $z = 1$ to $z = 0.5$, and it remains unchanged until $z = 0$.

The evolution of the radial profile in the SSPH run is

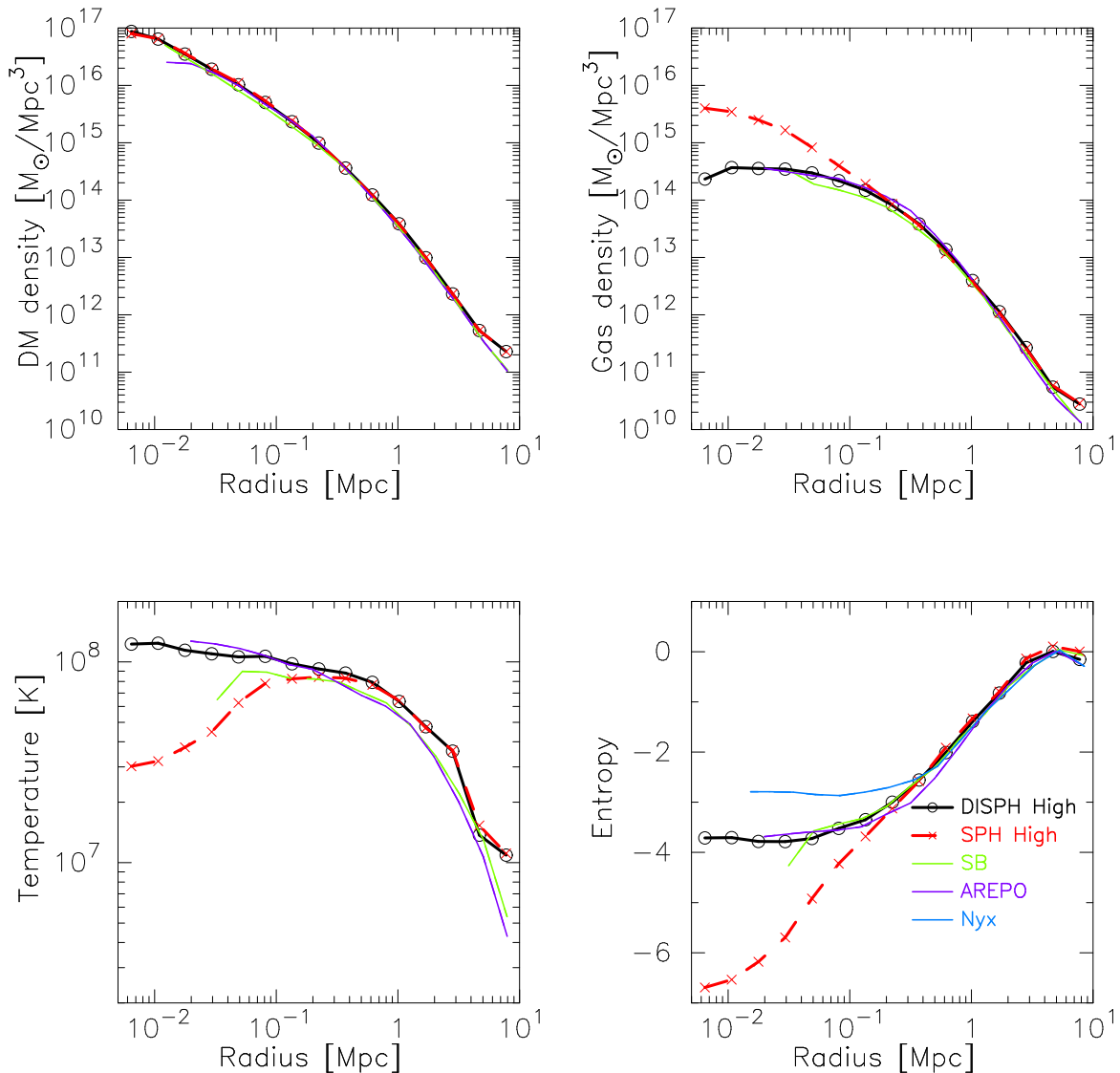


FIG. 4.— Radial profiles of the cluster at $z = 0$ for the high resolution runs and several reference results. Top-left, top-right, bottom left, and bottom right panels show the DM density, gas density, temperature, and entropy profiles, respectively. Solid black and dashed red curves are the profiles with the high resolution DISPH and SSPH. Solid, thin curves with light-green, purple, regatta-blue are the averaged profiles of Frenk et al. (1999) (from figure 18 in their paper), the profiles of the moving mesh code AREPO (Springel 2010) (from figure 45 in his paper. We adopt the result labeled 128³), and the profiles of an AMR code Nyx (Almgren et al. 2013) (from figure 7 in their paper), respectively. The AMR result is only shown in the entropy panel.

quite different from that in the DISPH run. At $z = 1$, the entropy profile with SSPH has a small core which is comparable to that of the DISPH run. This entropy core becomes larger until $z = 0.5$. However the core entropy is much lower than that with the DISPH run. At $z = 0$, the entropy core vanishes nearly. The density profile follows this evolution similarly but in the opposite direction. At the end of the simulation the density profile has a cusp.

Evolution of the radius of the entropy core and the averaged core entropy in the runs with DISPH and SSPH are shown in figures 8 and 9. The definition of the core radius is described in appendix C. The averaged core entropy is measured using the entropy of gas in the core radius. Their evolutions can be divided into two phases and the transition takes place after the major merger epoch ($z \sim 0.5$).

In the DISPH runs, two results agree with each other

very well. In the early phase ($z \geq 0.5$), the radius of the entropy core increases from ~ 20 kpc ($z \sim 3$) to 100 kpc ($z \sim 0.5$) and the averaged core entropy increases from -7 ($z \sim 3$) to -4 ($z \sim 0.5$). Then the growth of the core radius is stopped and the core is essentially unchanged until $z = 0$.

In the SSPH runs, the evolution is completely different from those of DISPH runs. When we compare the high resolution runs, the core radius of the SSPH run is smaller than that of the DISPH run in the initial phase ($z \geq 0.5$). Major merger triggered the rapid increase, but at $z \sim 0.5$ the core is still smaller than that of DISPH runs. Second, the core size shrinks and the averaged core entropy decreases in the late phase ($z \leq 0.5$). These figures suggest that the low-entropy material is supplied to the central region, most likely via minor mergers in the late phase. The low resolution SSPH run follows the

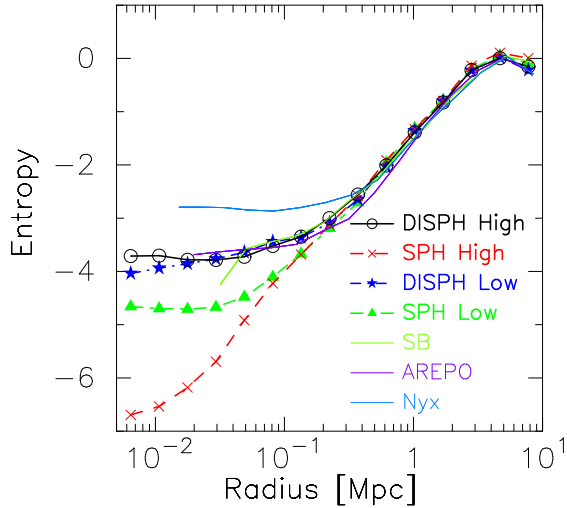


FIG. 5.— Comparison of radial entropy profiles of the cluster at $z = 0$. The solid (black) and dashed (red) curves are the high resolution runs with DISPH and SSPH, whereas the dot-dashed (blue) and dot (green) curves are the low resolution runs with DISPH and SSPH. The other thin, solid curves are the same as those in the top-right panel in figure 4.

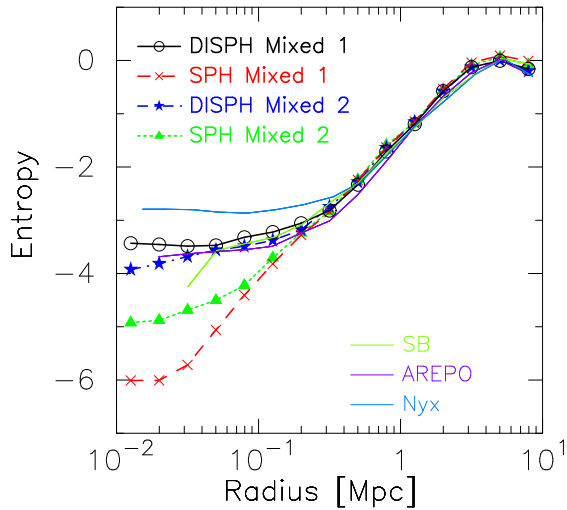


FIG. 6.— Same as figure 5, but for mixed resolutions. The solid (black) and dashed (red) curves represent the run of the mixed resolution 1 with DISPH and SSPH, whereas the dot-dashed (blue) and dot (green) curves indicate the results of the mixed resolution 2 with DISPH and SSPH. The reference curves are also shown.

evolution of the high resolution one, although it goes between DISPH runs and the high resolution SSPH runs because of lower resolution.

In §4.4.1 and §4.4.2, we further investigate the evolution of the cluster’s central entropy induced by the major and minor mergers.

4.4.1. Change of Core Entropy by Major Merger

Figure 10 shows the evolution of the distributions of pressure and entropy in the cluster in the high resolution DISPH run during the major merger phase ($0.75 > z > 0.52$). A smaller cluster consisting of the low-entropy material approaches from the top-right corner ($z = 0.75$), it merges with the main cluster ($z = 0.70$) and after several crossing times these two clusters completely merge to form a single cluster with the relaxed structure ($z = 0.63$ and $z = 0.52$). In this run, the entropy at the cluster cen-

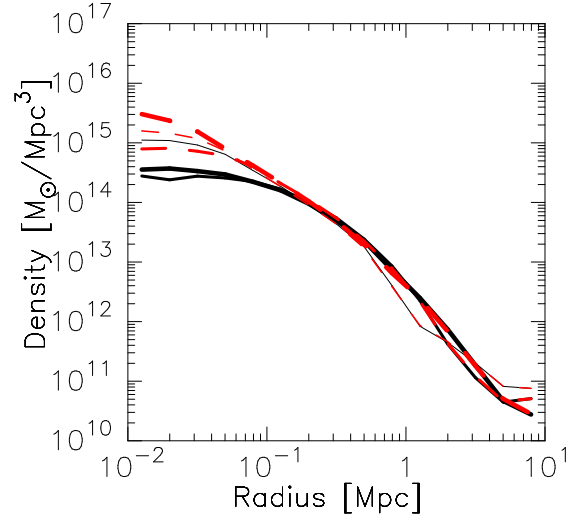
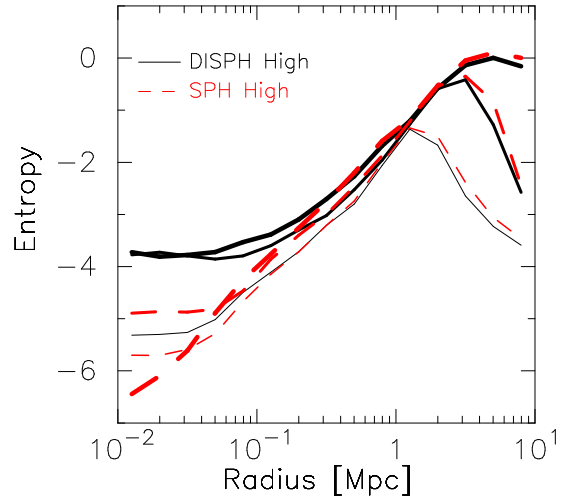


FIG. 7.— Radial entropy (top) and density (bottom) profiles of high resolution runs with DISPH/SSPH at three different epochs. Thin, normal, and thick curves are the radial entropy profiles at $z = 1$, $z = 0.5$ and $z = 0$, respectively. Solid curves are for the high resolution DISPH run, whereas dashed ones are for the high resolution SSPH run.

ter increases due to shocks (see bottom panels). Before the merging event, the central entropy is lower than -4 , but it becomes higher than -4 after the merger event (See also figure 9, $s \sim -4.4$ at $z \sim 0.74$ whereas $s \sim -4$ at $z \sim 0.5$). The pressure maps are smooth throughout this event (Top panels).

In the SSPH run, we also observe the increase of the central entropy whereas the absolute value is lower than that in the DISPH run, as we see figure 11. There are sharp edges in the distribution of the low-entropy (cold) gas clumps, and therefore the mixing of low- and high-entropy components is much weaker in the SSPH run compared to that in the DISPH run. Pressure maps show sharp gaps which are not found in those in the DISPH run. Thus, these gaps are outcomes of the unphysical surface tension of SSPH, resulting in the suppression of the entropy generation due to shocks.

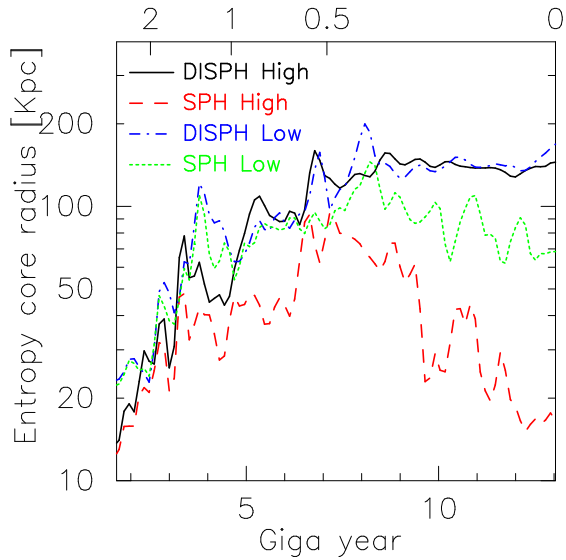


FIG. 8.— Entropy core radius as a function of the cosmic age. The corresponding redshift is also shown (the digit above the panel). Eq C1 is used in order to measure the core radius. The solid (black), dashed (red), dot-dashed (blue), and dotted (green) curves are the results with the high-resolution DISPH, the high-resolution SSPH, the low-resolution SSPH, and the low-resolution DISPH, respectively.

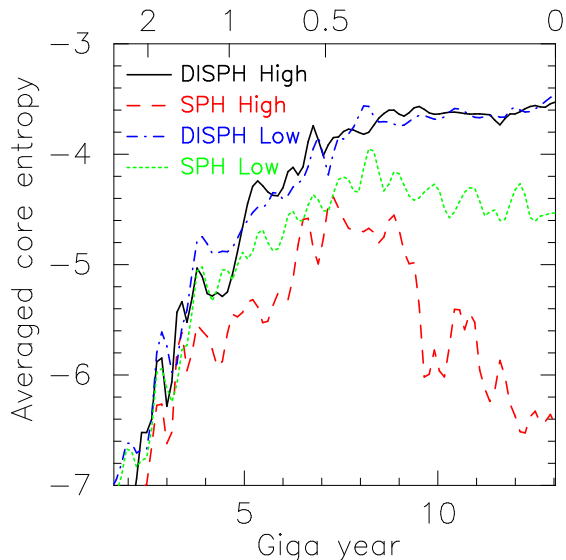


FIG. 9.— Averaged core entropy as a function of the cosmic age. The averaged core entropy is calculated using particles in the core radius. The corresponding redshift is also shown above the plot panel. Types of curves are the same as figure 8.

4.4.2. Change/Non-change of Core Entropy by Minor Mergers

Here, we focus on the late stage of the evolution of the cluster. Figure 12 shows the evolution of the radial entropy distribution. The main sequence of the entropy distribution, where the relative fraction is high, corresponds to the radial entropy profile we saw in, e.g., figure 5. In addition to the main sequence, there are a number of low entropy components. These low-entropy components are clumps in and around the cluster.

The evolution of the cold gas clumps are quite different in the DISPH run and SSPH run. In the case of

SSPH run (bottom panels), there are many clumps with minimum entropy around -8 , within the distance range $0.1 \text{ Mpc} - 1 \text{ Mpc}$. On the other hand, in the case of the DISPH run, there are only a few clumps within the distance 1 Mpc , and their minimum entropy is much higher. Thus, in the case of the SSPH runs, cold gas clumps survive in the cluster and fall to the cluster center, forming low-entropy core, while in the case of the DISPH run, cold gas clumps are disrupted before they reach to the center of the cluster.

In order to clarify the difference of the late stage evolution of the DISPH run and that of the SSPH run, we here focus on the evolution of one clump. For this analysis, we first pick up low entropy component within R_{200} . The threshold entropy is -4.5 which is slightly lower than the core entropy of the DISPH runs at $z = 0$. With this threshold, we found a number of low entropy clumps. In order to select one representative clump from them, we imposed the following conditions: (1) the clump is approaching to the cluster center, (2) the mass is sufficiently large so that we can track its evolution, (3) the clump reaches to the center of the cluster before $z = 0$, and (4) the clump can be found in both runs at the same position. The representative clump we picked up is found at $R_d \sim 1.7 \text{ Mpc}$ and its total mass is $\sim 10^{13} M_\odot$ at $z = 0.12$.

Figure 13 shows the evolution of this low-entropy clump in the high-resolution DISPH run. From the particle distribution maps (upper panels), we can see that this representative clump enters the cluster center forming a bow-shock. Its front surface is being stripped due to fluid instabilities, resulting in the complete destruction of the clump by $z = 0.04$ (recall the blob test in Agertz et al. 2007). The pressure distribution across the interface between the clump and the intracluster medium is always smooth.

Figure 14 shows the evolution of the same clump in the high-resolution SSPH run. There is a clear gap both in the particle and pressure distributions in the front of the clump. This gap is induced by the unphysical surface tension, protecting this clump from the development of fluid instabilities at the surface and ram-pressure stripping. Thus, the low entropy gas in this clump can sink to the cluster center.

We compare the evolutions of this representative clump in DISPH and SSPH runs in figure 15. Top, middle, and bottom panels are the distance from the cluster center, the size, and the averaged entropy of the gas particles of the clump, respectively. Before the pericenter passage, clumps in two runs are almost identical. When it passed the pericenter, the orbital decay starts. The orbital decay in the SSPH run is much faster than that in the DISPH run. Clumps expand when passing the pericenter. The clump in the DISPH run is more extended compared to that in the SSPH run. These two results tell us that the clump in the SSPH run keeps a compact structure much longer.

The increase of the mean entropy starts slightly before the pericenter passage in both runs. At $z = 0$, the mean entropy of the clump in DISPH is ~ 1 higher than that in SSPH. This indicates that the shock heating is more efficient in the DISPH run. However, behind the fact that SSPH has unphysical surface tension, we should say that the shock heating in SSPH is more inefficient. DISPH

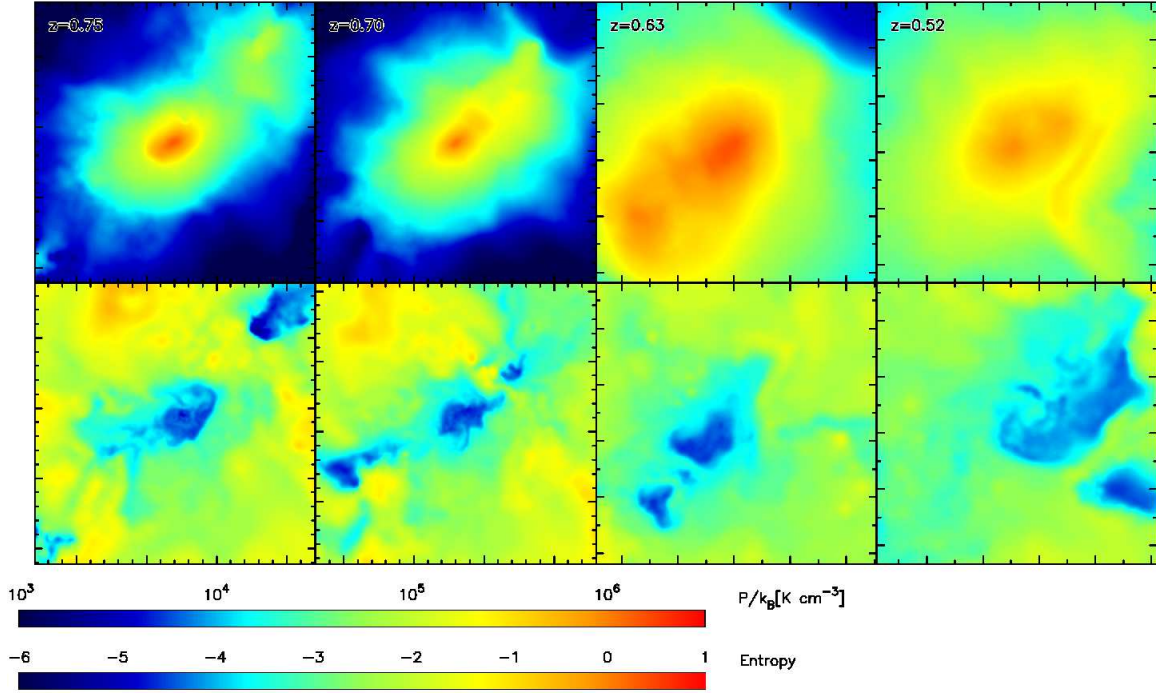


FIG. 10.— Evolution of the cluster for the high resolution DISPH run during the major merger phase. Top and bottom panels show the distributions of pressure and entropy at the XY plane which across the density center evaluated by Eq (6). The plot regions of the left two columns are $4 \text{ Mpc} \times 4 \text{ Mpc}$ whereas those of the right two columns are $2 \text{ Mpc} \times 2 \text{ Mpc}$. The epoch (redshift) is displayed on the top-left corner of each panel of pressure map.

can capture the intrinsic shocks. This difference in the shock heating efficiency explains why cold gas clumps can reach to the center of the cluster in the SSPH run but are disrupted in the DISPH run.

This tendency that the clumps in the SSPH run survive longer at the center of the cluster compared to those in the DISPH run can be seen in figure 16. Here, we used subfind clumps (see appendix D) and stacked data during $0 \leq z \leq 0.12$ (total 17 snapshots). Generally, as clumps move closer to the center of the cluster, they lose their masses due to tidal and ram-pressure stripping. At the same distance from the cluster center, in particular for $R < 1 \text{ Mpc}$, we can see the clear tendency that clumps in SSPH are more massive than those in DISPH. Thus, the evolution of the inner part of the cluster strongly affected by the choice of the SPH scheme. While clump surviving time is different, there is no significant difference in mass functions with different SPH schemes (see appendix E).

It has been pointed out by Power et al. (2014) that the cluster core entropy decreased at the low- z with SSPH. They measured the evolution of entropy at the central region ($0.01 \times R_{200}$) of clusters of galaxies in a Λ CDM universe. They found that the core entropy of the SSPH run decreased continuously for $0 < z < 0.6$ whereas those of AMR and SPHS runs were roughly constant. Although they did not follow the individual clumps, they explained that the change of the central entropy found in low- z period is due to the accretion of the low-entropy clumps induced by the minor mergers. Our study supports their result and this process works in the evolution of the Santa Barbara cluster in previous studies as well.

4.5. Effects of Artificial Conductivity Term

Recently, the AC term has become widely used in SPH simulations in order to remove the unphysical surface tension (e.g., Price 2008; Rosswog 2009; Read & Hayfield 2012; Kawata et al. 2013; Beck et al. 2016). Here, we investigate the effects of AC on the cluster formation and evolution. Similar studies are found in the literature (e.g., Wadsley et al. 2008; Power et al. 2014; Biffi & Valdarnini 2015; Hopkins 2015; Beck et al. 2016; Sembolini et al. 2016).

According to the numerical experiments by Wadsley et al. (2008) and Power et al. (2014), it is expected that the entropy core appears if the AC term is introduced into SSPH and the core size and core entropy depend on the maximum value of the conduction control parameter $\alpha_{AC, \max}$. Thus, in this section, we highlight the contribution of $\alpha_{AC, \max}$ to the thermal structure and the entropy profile.

Here, we adopt the following functional form for the AC:

$$\frac{du_i}{dt} = \sum_j m_j \frac{4\alpha_{AC,i}\alpha_{AC,j}}{\alpha_{AC,i} + \alpha_{AC,j}} \frac{v_{\text{sig},ij}^u}{\rho_{ij}} (u_i - u_j) \nabla W_{ij}, \quad (8)$$

where $\rho_{ij} = 0.5(\rho_i + \rho_j)$, $v_{\text{sig},ij}^u = \sqrt{|P_i - P_j|/\rho_{ij}}$, P is pressure, and $\nabla W_{ij} = 0.5[\nabla W(\mathbf{x}_j - \mathbf{x}_i, h_i) + \nabla W(\mathbf{x}_i - \mathbf{x}_j, h_j)]$. Following Beck et al. (2016), we evaluate the AC coefficient of particle i , $\alpha_{AC,i}$ using the following equation;

$$\alpha_{AC,i} = \frac{h_i}{3} \frac{|\nabla u_i|}{|u_i|}, \quad (9)$$

where ∇u_i is evaluated by the SPH manner and $\alpha_{AC,i}$ is allowed to evolve from 10^{-5} to $\alpha_{AC, \max}$. This AC term is essentially the same as those adopted in the previous

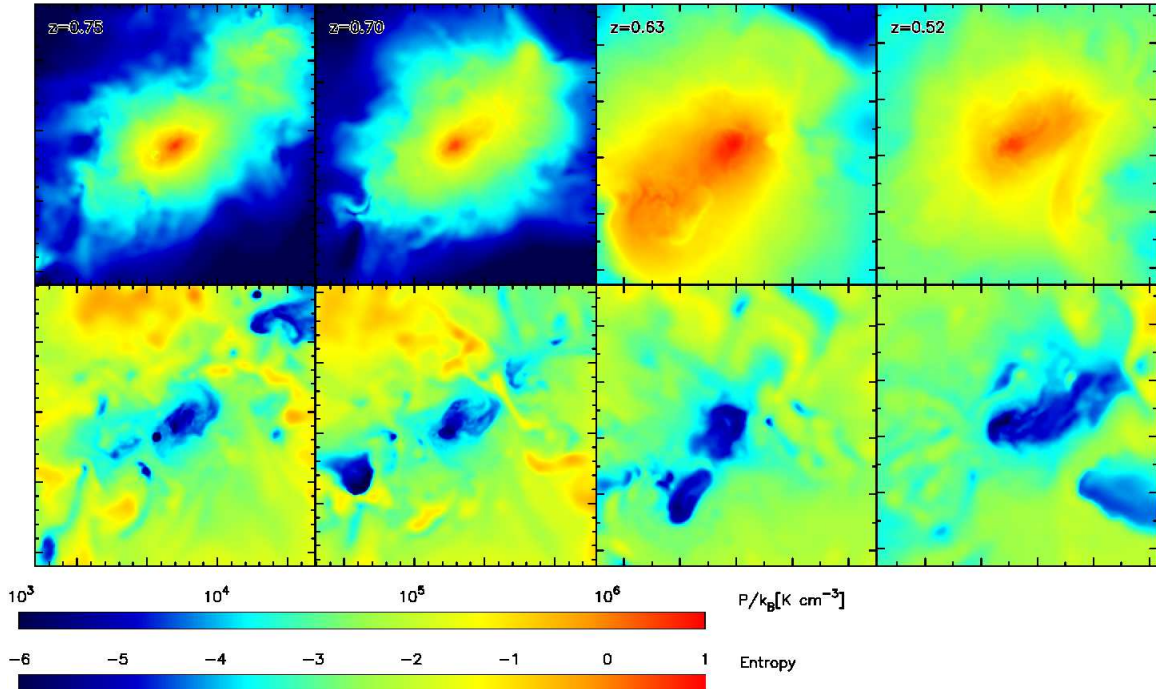


FIG. 11.— Same as figure 10, but for the high-resolution SSPH run.

studies (e.g., Price 2008; Rosswog 2009; Read & Hayfield 2012; Power et al. 2014; Hu et al. 2014; Hopkins 2015; Beck et al. 2016). We tested several functional forms and switches and found that the conclusion in this subsection does not affected by them. We show five high-resolution SSPH runs with different values of $\alpha_{AC,max}$: $\alpha_{AC,max} = 0.01, 0.1, 0.25, 1$ and 5 .

Figure 17 shows the temperature maps of five runs with the AC term, as well as that of the run without AC. From this figure, we can see that the temperature structure gets blurred when $\alpha_{AC,max}$ increases. We find that there is a similar effect in both the density and entropy maps. This blurring effect has an influence on the entropy profile of the cluster, as we see next.

Figure 18 shows the radial entropy profiles with and without AC. Apparently, the entropy profile is affected by AC. The entropy profile with $\alpha_{AC,max} = 0.01$ is cuspy; it has a slightly higher entropy than that without AC in $R < 200$ kpc. On the other hand, those with $\alpha_{AC,max} \geq 0.1$ have cores. These core entropies increase with increasing $\alpha_{AC,max}$ and the increase stalls when $\alpha_{AC,max} \geq 1$. The core entropy with $\alpha_{AC,max} = 0.1$ is comparable to those with DISPH and AREPO whereas that with $\alpha_{AC,max} = 5$ is rather close to that obtained by a mesh code. In our test, unlike previous study (Beck et al. 2016), the core entropies with $\alpha_{AC,max} \geq 1$ are slightly lower than those obtained by mesh codes. This difference might come from the detailed implementations.

Time evolutions of averaged core entropies for five AC runs are shown in figure 19. The overall evolutions of the runs with $\alpha_{AC,max} \geq 0.1$ are similar to those of DISPH runs; the increase of the core entropy is fast until $z \sim 0.5$ and then it stops. On the other hand, the evolution with $\alpha_{AC,max} = 0.01$ is close to that without AC, whereas this run has a slightly higher entropy within 200 kpc.

The final core sizes are 220–280 kpc for the runs with $\alpha_{AC,max} \geq 0.1$ (Recall that they are ~ 150 kpc in DISPH runs).

Although SSPH runs with AC ($\alpha_{AC,max} \geq 0.1$) have slightly larger entropy cores, the effect of the AC term looks similar to that of DISPH; the essential difference is that AC requires the new free parameter $\alpha_{AC,max}$. Since the numerical results depend on this parameter, one needs to pay attention to determine its value. It is of course possible that the calibrated $\alpha_{AC,max}$ for one experiment is inadequate for another experiment.

5. SUMMARY & DISCUSSION

In this paper, we studied the formation of the entropy core in the Santa Barbara cluster. Previous studies (e.g., Frenk et al. 1999; Kravtsov et al. 2002; Springel 2005; Almgren et al. 2013) have demonstrated that simulations with Eulerian mesh codes make the entropy core in the cluster center while those with Lagrangian SPH codes do not. The original paper (Frenk et al. 1999) argued that the origin of this difference came from the different treatment of shocks in the SPH and mesh codes. However, both Eulerian mesh codes and Lagrangian SPH codes have their own, intrinsic limitations which might affect the entropy evolution. This implies that neither mesh results nor SPH results is correct. Springel (2010) and Hopkins (2015) reported that new Lagrangian fluid schemes made entropy cores but the depth of their cores is deeper than those obtained by Eulerian codes.

The clusters simulated with DISPH formed prominent entropy cores and its size and absolute value of the core entropy was insensitive to the adopted resolutions. During the cluster formation, a number of low entropy clumps accreted and these clumps brought low entropy materials to the cluster center. In the DISPH runs, the ram pressure stripping and fluid instabilities disrupted these clumps efficiently in DISPH runs. The entropy of

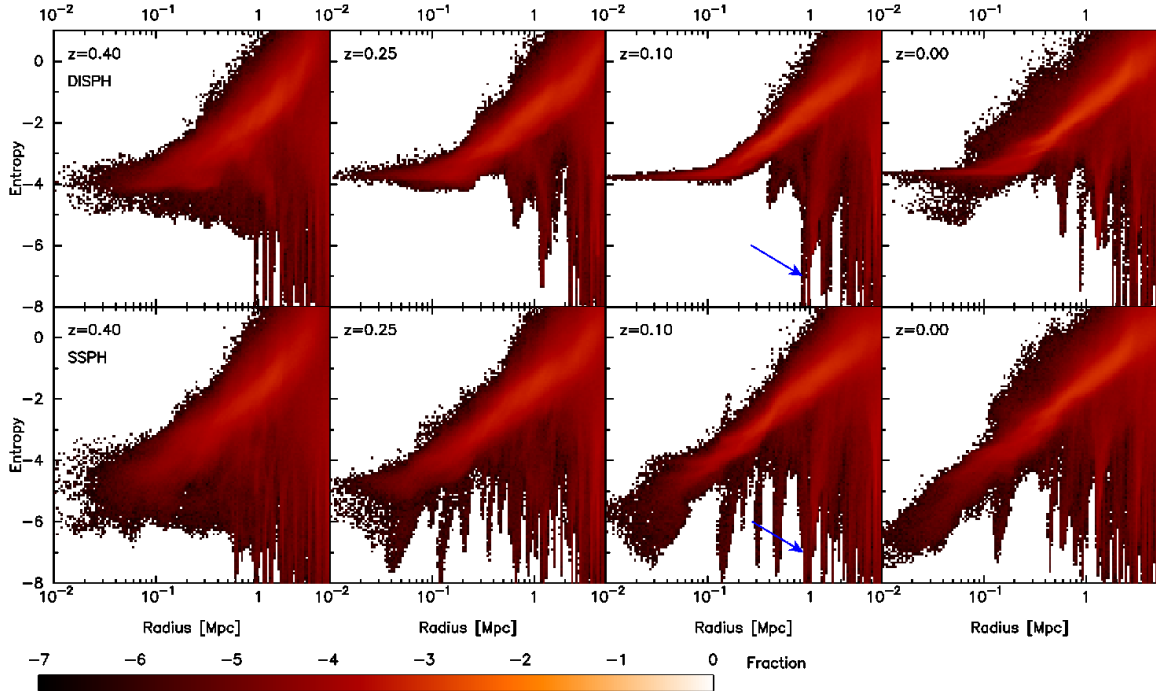


FIG. 12.— Evolution of radial entropy distributions. Top panels show the results of the high resolution DISPH run, whereas bottom panels represent those of the high resolution SSPH run. Colors correspond to the relative fraction of particles in the logarithmic scale. Blue arrows on the panels of $z = 0.1$ point the positions of the representative clumps (see text).

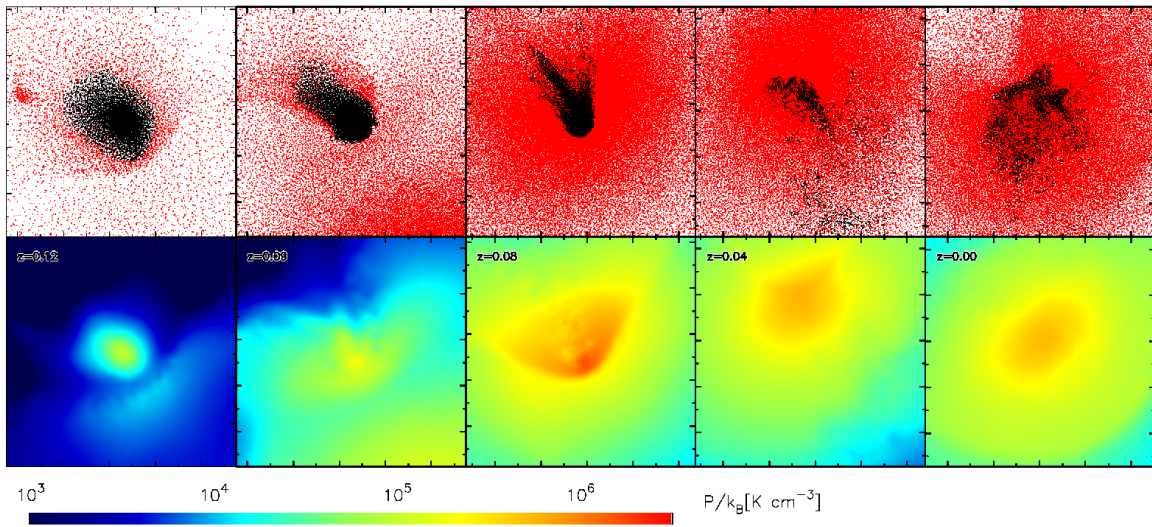


FIG. 13.— Evolution of the low entropy clump in the high-resolution run with DISPH. Top panels show the distributions of particles initially associated with the low-entropy clump (black) and the others (red). The coordinates center is set to the baricenter of the clump and the regions of $1 \text{ Mpc} \times 1 \text{ Mpc}$ are plotted. The particles shown in the upper panels are selected from particles in the thickness of $Z = \pm 0.1 \text{ Mpc}$. Bottom panels display the pressure maps at the $Z = 0$ plane. The time from the left to right panels is $\sim 2 \text{ Gyr}$.

these clumps increased due to hydrodynamical shock and they built the entropy core.

The size of the entropy core at $z = 0$ is $\sim 150 \text{ kpc}$ and the depth of that is $s \sim -4$. These values are comparable with those obtained by the original version of the moving mesh code (Springel 2010) and the mesh free code (Hopkins 2015). The values of the core entropy obtained in these simulations are about unity lower than those with Eulerian mesh codes. This systematic difference is probably due to the numerical diffusion intrinsically existing in Eulerian codes (e.g., Tasker et al. 2008; Springel

2010). In principle, the effect of the numerical diffusion can be reduced by increasing the spatial resolution (Robertson et al. 2010). However, whether this strategy is really useful for cosmological simulations or not is unclear since this approach is quite time-consuming.

We were able to reproduce the cuspy entropy profile when we used SSPH and the results with SSPH depended strongly on the adopted mass resolution. When we employ low mass resolution, there is a small core which is comparable with the previous simulations. When we adopt the high mass resolution, the central entropy be-

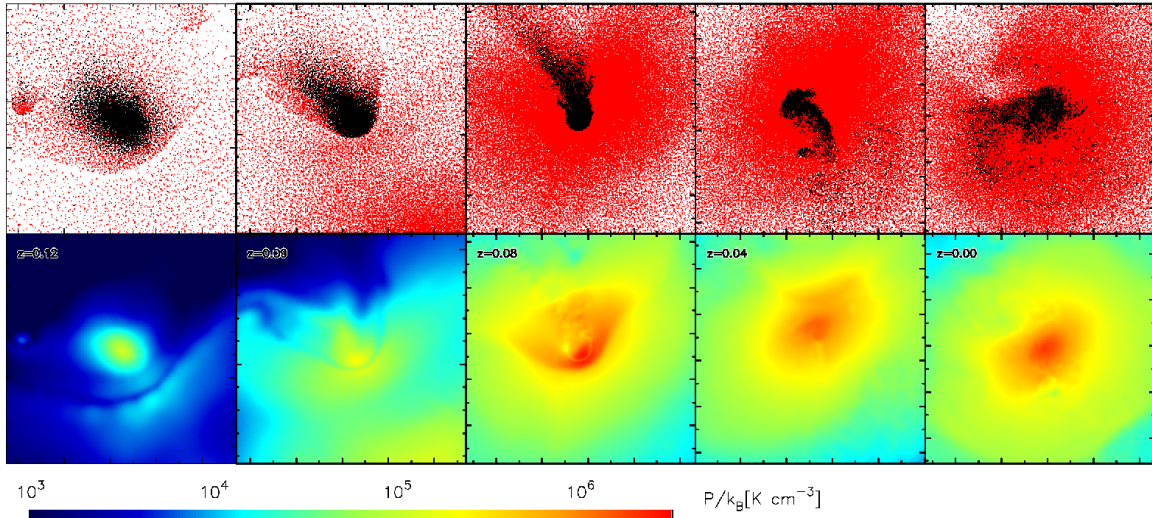


FIG. 14.— The same as figure 13, but for the high-resolution SSPH.

came much lower and the cuspy profile appeared. By following the evolution of the central entropy, we found that the central entropy in SSPH runs affected by the minor mergers involving the low-entropy gas. Low-entropy gas in simulations with SSPH is “protected” against ram-pressure stripping, as found by Agertz et al. (2007). The evolution of low-entropy clumps in DISPH is completely different from that in SSPH. The cuspy entropy profile found in the SSPH runs is artifact.

We can obtain the entropy core in the Santa Barbara cluster with just changing the volume element of the formulation and without introducing any diffusions. There are several studies in which entropy core was obtained by introducing dissipations to SPH (Wadsley et al. 2008; Read & Hayfield 2012; Biffi & Valdarnini 2015; Beck et al. 2016). In their studies, they could obtain cored entropy profiles. We also confirmed it by our numerical experiments. As is reported by previous studies, the core size depended on the diffusion coefficient of the conductivity. Our method has advantages over these methods since there is no need to calibrate the diffusion coefficients. In addition, there is no time and spatial scales which controls the degree of the dissipation strength if we used DISPH, since formulation of DISPH itself can remove the unphysical surface tension. We thus conclude that DISPH is a good alternative to SSPH for the cosmological structure formation.

There is room to improve the implementation of the AV term and switches. For instance, a sophisticated switch is important in order to deal with a rotating system (Cullen & Dehnen 2010). Recently, Hosono et al. (2016a) showed a survey of the implementation of the AV. In their study, they showed that the run with the combination of the von-Neumann-Richtmyer-Landshoff type AV term velocity gradient (García-Senz et al. 2012; Hu et al. 2014; Rosswog 2015) can maintain the Keplerian disk for ~ 100 orbits. We need to investigate the feasibility of these methods in structure formation simulations.

We thank the anonymous referee. Her/his insightful comments improve our manuscript greatly. T.R.S.

thanks Takashi Okamoto and Kohji Yoshikawa for useful discussion. T.R.S. also thanks Lucy Kwok and Junko Saitoh who helped in writing the manuscript. Numerical simulations were carried out on the Cray XC30 system in the Center for Computational Astrophysics at the National Astronomical Observatory of Japan. This work is supported by Grant-in-Aid for Scientific Research (26707007) of Japan Society for the Promotion of Science and Strategic Programs for Innovative Research of the Ministry of Education, Culture, Sports, Science and Technology (SPIRE). This work is supported in part by MEXT SPIRE and JICFuS.

APPENDIX

A. DIFFICULTIES OF AC TERM FOR A FLUID CONSISTING OF DIFFERENT CHEMICAL COMPOSITIONS

The philosophy of the introduction of AC is to ensure all physical quantities will be smooth everywhere. At a contact discontinuity, SSPH makes a pressure blip if the internal energy does not have a smoothed profile consistent with the smoothed profile of density. To guarantee the consistent profile of the internal energy, AC spreads the internal energy until the pressure profile becomes smooth. This term works very well in the standard tests and widely used. However, one meets a difficulty when one applies AC to a contact discontinuity consisting of a fluid with different chemical compositions.

Consider the case in which there are two contacting fluids and they have different chemical compositions. Here, we assume that they have different mean molecular weights, μ . Thus, the internal energy is a function of μ and temperature T ; $u = u(\mu, T)$. Moreover, these two fluids are initially in the pressure and temperature equilibrium state. DISPH can reproduce the original pressure and temperature equilibrium state without any difficulty. On the other hand, SSPH cannot reproduce it; a pressure jump appears across the contact interface. SSPH with the AC term gives a pressure equilibrium state by changing the internal energy of particles around the contact interface.

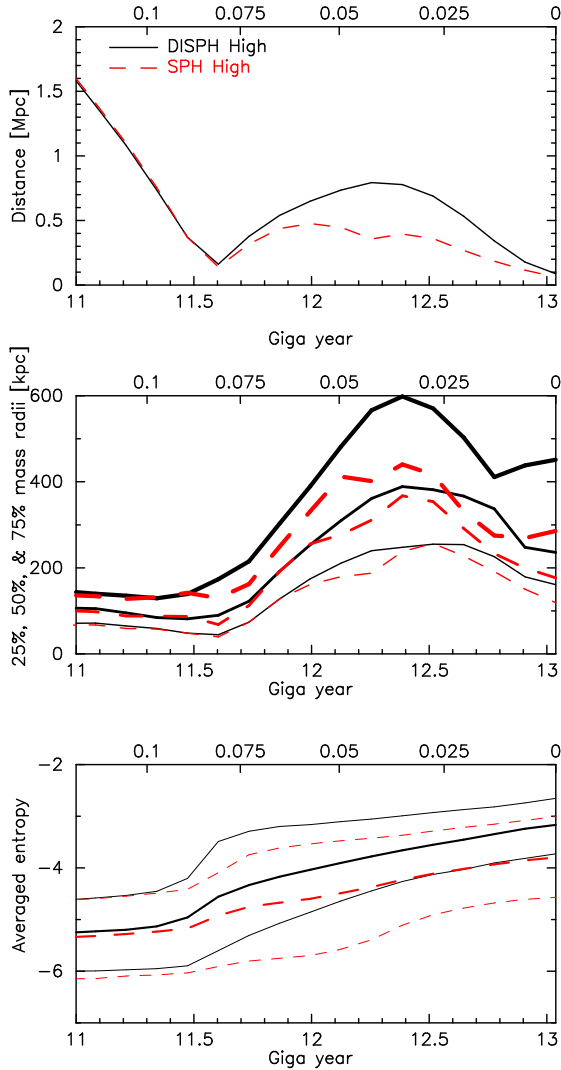


FIG. 15.— Time evolutions of the distance from the center of the cluster, the size and the mean entropy of the representative clump. Top: Distance between the entropy weighted center of the representative clumps and the density peak of the halo. Middle: 25% (thin curve), 50% (normal curve) and 75% (thick curve) radii from the clump center. Bottom: Mean entropies of the gas in the representative clumps (thick curves). Thin curves for each run represent 10% and 90% spread of the entropy distribution.

Since $u = u(\mu, T)$, this change of u induced by AC is regarded as the changes of T and μ . Unfortunately, we do not know an appropriate procedure to spread T and μ . Hence, we cannot predict exact quantities of μ and T at the contact interface. There are two possible limits: (1) T changes but μ does not, and (2) μ alters but T does not. The former leads to undesirable chemical reactions if one is solving the chemical reactions, since they depend on T . The latter is the compulsive mixing of chemical compositions.

We show a simple, one-dimensional numerical experiment regarding this problem. The initial condition is as follows. The computational domain is $0 \leq x < 1$ with a periodic boundary condition. The fluid at $0.25 \leq x < 0.75$ has $\mu_1 = 1$ while the other has $\mu_2 = 2$. Both pressure and temperature have constant values in the whole region. Since $\mu_1 \neq \mu_2$, the density and internal energy have different values in these two sub-domains. Here the

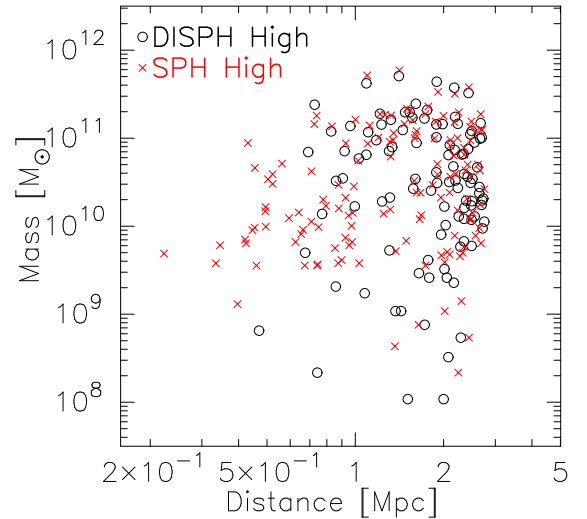


FIG. 16.— Masses of the gas component in subfind clumps as a function of the distance from the cluster center. We stacked clumps within R_{200} from $z = 0.12$ to $z = 0$. Total number of the snapshots is 17 and the time interval between two closest snapshots are ~ 130 Myr. Open circles are for the high-resolution DISPH run whereas crosses are for the high-resolution SSPH run.

initial pressure and temperature are unity and $\gamma = 5/3$. The density is normalized so that $\rho = \mu$. We solved this system until ~ 100 sound crossing time. We used two schemes: one was DISPH and the other was SSPH with the AC term. Here, we adopt the AC term described in §4.5 and $\alpha_{AC, \max} = 1$.

Figure 20 shows the results of SSPH with the AC term and DISPH at time 100 (about 100 crossing time). In the SSPH run with the AC term, the initial pressure jump is smeared by smoothing the distribution of the internal energy (the top-right panel in figure 20). If we consider this change of the internal energy as the change of the temperature, we have the temperature distribution with jumps at the contact discontinuities shown in the middle-right panel. On the other hand, if we regard it as the change of μ , we obtain the smoothed distribution of μ as shown in the bottom-right panel. In DISPH, there is no difficulty in dealing with this system (panels in the left column).

A system consisting of materials with different chemical compositions is not an unphysical situation. For instance, for a giant impact simulation, one solves collisions of core(iron)-mantle(silicon based rock) planet embryos (Benz et al. 1987; Cameron 1997; Canup & Asphaug 2001; Canup 2004; Nakajima & Stevenson 2014; Hosono et al. 2016b). At the core-mantle boundary, there is a jump of the composition. In addition, at the contact interface at the colliding time there is also a jump of the chemical composition. If we use the AC term for this simulation, the boundary materials are mixed and/or the temperature at these boundaries changes. DISPH for a non-ideal gas (Hosono et al. 2013) can deal with these boundaries without any difficulty (Hosono et al. 2016b).

B. TIME INTEGRATION SCHEME AND BENCHMARK TEST

The time integration of a single step from n -th step to $(n + 1)$ -th step where the time step is Δt is carried out

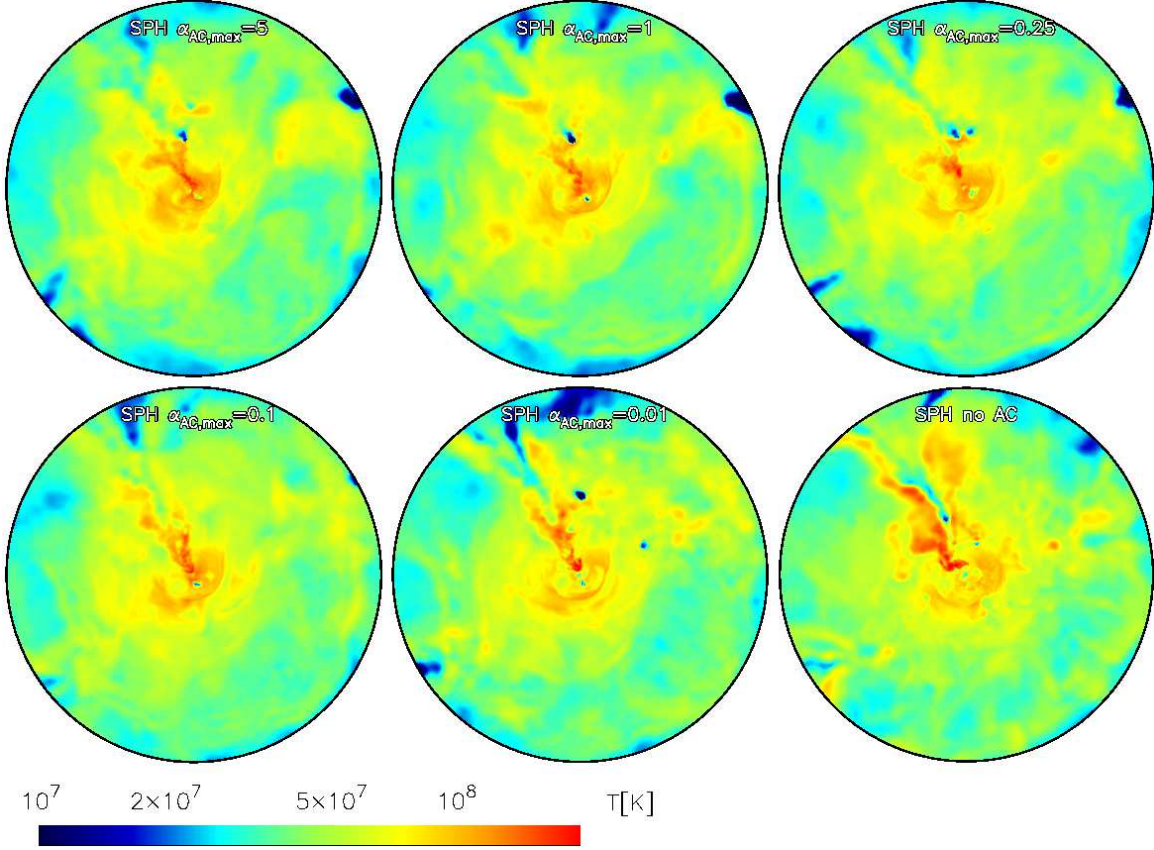


FIG. 17.— Temperature maps of SSPH runs with the AC term at $z = 0$. Results with five different values of $\alpha_{AC,max}$ are displayed. The result without AC term is also shown as a reference. The plotted region corresponds to the virial radius.

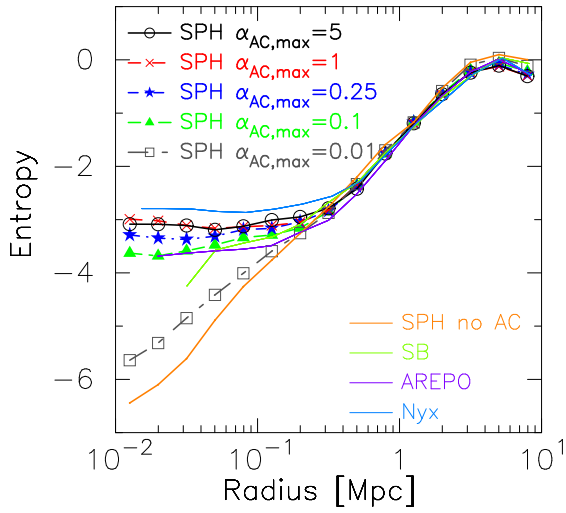


FIG. 18.— Radial entropy profiles of SSPH runs with the AC term at $z = 0$. Those without the AC term and obtained from literatures are also shown.

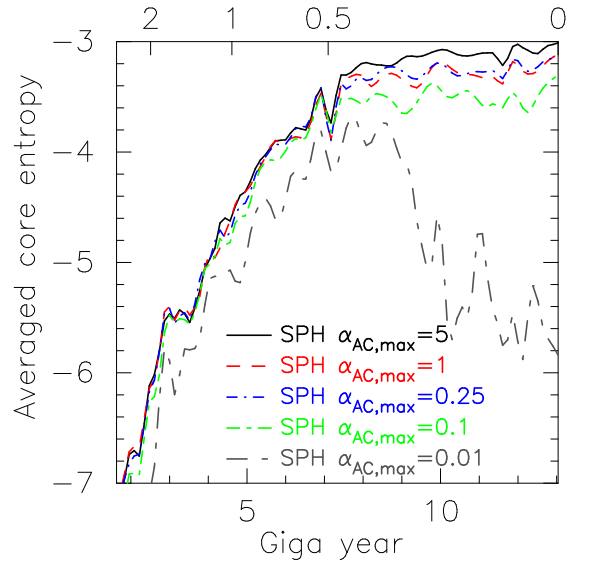


FIG. 19.— Averaged core entropy as a function of the cosmic age. Results of five AC runs are shown.

by the following procedure:

1. Advance the velocity \mathbf{v}^n from n -th step to $(n+1/2)$ -th step using the acceleration \mathbf{a}^n :

$$\mathbf{v}^{n+1/2} = \mathbf{v}^n + \frac{1}{2}\mathbf{a}^n\Delta t. \quad (\text{B1})$$

2. Drift the position \mathbf{x}^n from n -th step to $(n+1)$ -th

step using $\mathbf{v}^{n+1/2}$:

$$\mathbf{x}^{n+1} = \mathbf{x}^n + \mathbf{v}^{n+1/2}\Delta t. \quad (\text{B2})$$

3. Evaluate the predictor of the velocity at $(n+1)$ -th step using \mathbf{a}^n :

$$\mathbf{v}_p^{n+1} = \mathbf{v}^{n+1/2} + \frac{1}{2}\mathbf{a}^n\Delta t. \quad (\text{B3})$$

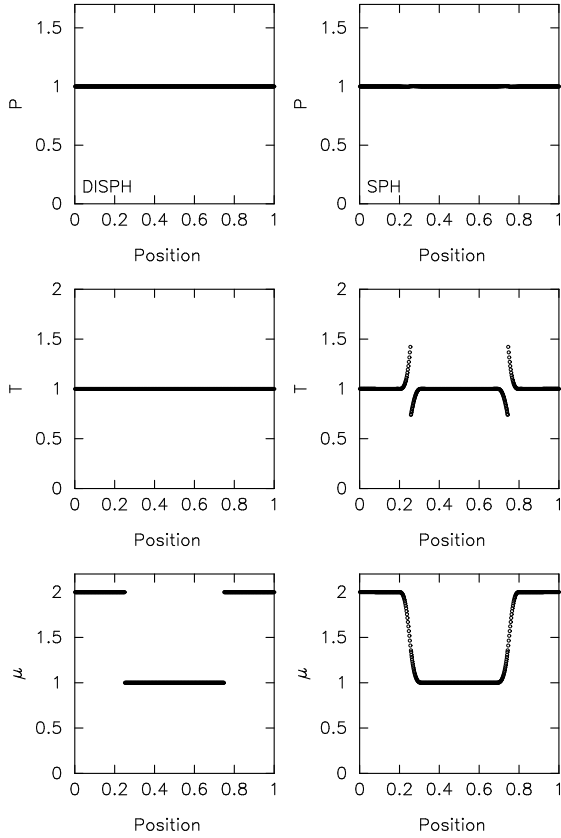


FIG. 20.— Distributions of P , T , and μ at time 100. Left and right columns show results of DISP and SSPH, respectively. For SSPH, we used with the AC term. Top and bottom are distributions of pressure and μ , respectively.

- Evaluate the predictor of the specific internal energy at $(n+1)$ -th step using the time derivative of u^n , du^n/dt :

$$u_p^{n+1} = u^n + \left(\frac{du}{dt}\right)^n \Delta t. \quad (\text{B4})$$

- Compute \mathbf{a}^{n+1} and du^n/dt using \mathbf{x}^{n+1} , \mathbf{v}_p^{n+1} , and u_p^{n+1} .
- Advance $\mathbf{v}^{n+1/2}$ by the rest of the half step using \mathbf{a}^{n+1} :

$$\mathbf{v}^{n+1} = \mathbf{v}^{n+1/2} + \frac{1}{2}\mathbf{a}^{n+1}\Delta t. \quad (\text{B5})$$

- Compute u^{n+1} using both du^n/dt and du^{n+1}/dt :

$$u^{n+1} = u^n + \frac{1}{2} \left[\left(\frac{du}{dt}\right)^n + \left(\frac{du}{dt}\right)^{n+1} \right] \Delta t. \quad (\text{B6})$$

The manner to integrate the internal energy described above is Heun's method (or the modified Euler's method or the second order Runge-Kutta method). Thus, our integration scheme is categorized as the second order method. For DM particles, this time integration scheme is reduced the standard second order symplectic scheme, the leap-frog scheme.

As a demonstration, we show the results of the adiabatic collapse test with this time integration scheme.

This test is one of the standard benchmark tests of self-gravitating fluid (Evrard 1988). A number of simulation codes showed results of this test (e.g., Hernquist & Katz 1989; Steinmetz & Mueller 1993; Springel 2005). The typical error of the total energy in this test is less than 1%.

The initial condition of this test was generated as follows. First, we prepared gas particles located on uniform grid points. Then, by stretching their relative distances from the center of the coordinates, we made the gas distribution with a radial density profile of $1/r$, where r is the distance from the center of the coordinates. The gas particles in $r < 1$ are adopted to make a gas sphere. We assumed that they do not have a bulk velocity at the beginning of the simulation. The total mass and the gravitational constant are unity. The specific initial thermal energy is 0.05 and $\gamma = 5/3$. Since the initial kinetic energy is zero and the thermal energy is less than the absolute value of the potential energy, this gas sphere collapses due to self-gravity and eventually reaches a state of equilibrium. Here, we represented this gas sphere with the 61432 equal-mass SPH particles. The gravitational softening length was set to 0.0034.

We carried out four runs. Two are DISP and SSPH, which were used in this paper. In these runs, the kernel size was determined so that the neighbor number is in the range of 128 ± 8 . However, it is pointed out that the use of the constant neighbor number often makes sudden change of the interaction radius, resulting in the fluctuations of physical quantities. Thus, the other two runs adopted the smoothed neighbor number method for the evaluation of kernel size (Springel & Hernquist 2002). Here, both DISP and SSPH were used. We express our fiducial cases as DISP and SSPH, and the other two cases with the smoothed neighbor number method as DISP(S) and SSPH(S).

The Wendland kernel C4 was adopted. The self-gravity was solved by using the tree with GRAPE method. The opening angle was set to 0.5. Time step for each particle is determined following Saitoh & Makino (2010).

Figure 21 shows the evolution of radial profiles of density, pressure, and radial velocity of the DISP run. Three representative epochs are adopted. Except for the central region ($r < 0.1$), our result is comparable with a 1D PPM result. The other three cases, SSPH, DISP(S), and SSPH(S), show almost identical results.

In figure 22, we show time evolutions of the kinetic, thermal, potential and total energies. Again, we show the result of the DISP run. The overall evolution is comparable with that obtained in previous studies and the other three cases show identical results.

Figure 23 represents time evolutions of the total energies in four runs.⁹ These total energies change significantly at time ~ 1 when the gas sphere collapses, while they keep almost a constant value at other times. We define the energy error as follows:

$$E_{\text{diff}} = \frac{|E_{\text{tot}}(3) - E_{\text{tot}}(0)|}{|E_{\text{tot}}(0)|}, \quad (\text{B7})$$

where $E_{\text{tot}}(0)$ and $E_{\text{tot}}(3)$ are the total energy of a system at time 0 and 3, respectively. Energy errors evaluated

⁹ We use SPH and SPH(S) in order to denote the results of SSPH and SSPH(S) in this figure.

by the above equation are 0.19% for DISPH, 0.22% for SSPH, 0.14% for DISPH(S), and 0.16% for SSPH(S), respectively. Thus our time integration scheme works well. The fact that there is no significant difference among them indicates that the choices of the definition of the neighbor numbers and SPH types are not crucial for the energy conservation in our simulations.

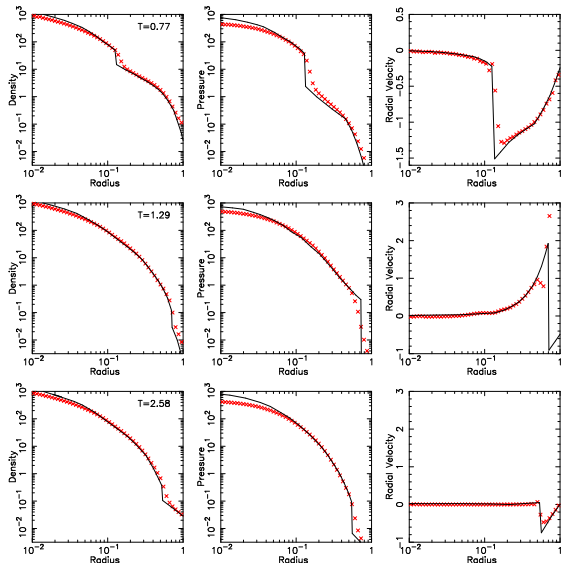


FIG. 21.— Radial profiles of three different epochs. From left to right, radial profiles of density, pressure and radial velocity are shown. According to Steinmetz & Mueller (1993), both the density and the pressure are normalized by a factor of $3/4\pi$. Red symbols represent the averaged quantities of the DISPH run with the bin width of 0.04 dex. Black curves represent the result of a 1D PPM calculation. These curves are obtained from figure 7 in Steinmetz & Mueller (1993). The DISPH run with the Wendland kernel C4 and $N_{\text{nb}} = 128 \pm 8$ is adopted.

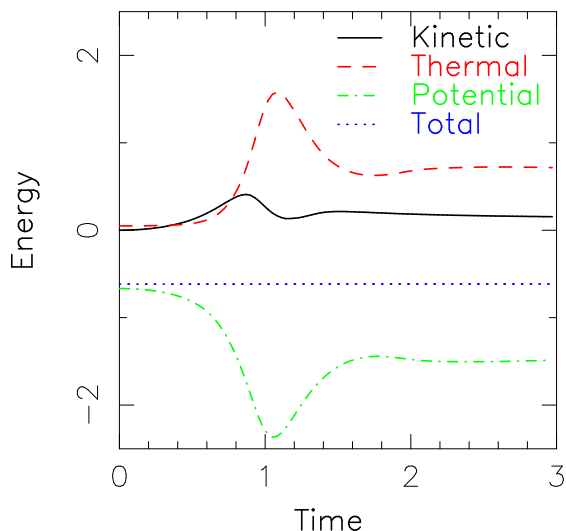


FIG. 22.— Kinetic, thermal, potential, and total energies as a function of time. The DISPH run with the Wendland kernel C4 and $N_{\text{nb}} = 128 \pm 8$ is adopted.

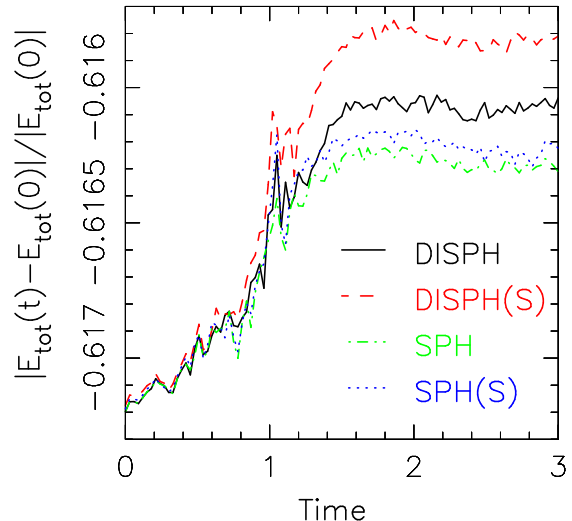


FIG. 23.— Total energies of four models as a function of time.

C. DEFINITION OF THE ENTROPY CORE RADIUS

In order to compare sizes of entropy core and their time evolutions among different simulations, we need a methodology to evaluate a core size from an entropy profile. As is shown in the text, the evolutions of core size and entropy are highly time-variable. In order to follow this dynamically evolving structure, we adopt the technique used in the field of stellar cluster simulation. Below, we describe our method to define the entropy core.

First, we calculate the radially averaged entropy profile; It is expressed as $s(R_d)$ ¹⁰, where R_d is the distance from the density center, \mathbf{x}_c . We, then, pick up particles of which entropy is in the range of $s(R_d) \pm 0.5$ and evaluate the core radius using these particles. The reason why we sampled particles from the narrow region is to exclude the contamination of small, low-entropy clumps (see also figure 12). Without this process, we were unable to obtain a reasonable size of the entropy core.

The following equation is used in order to evaluate the core radius:

$$R_{\text{core}} = \frac{\sum_k \exp(-4s_k) R_{d,k}}{\sum_k \exp(-4s_k)}, \quad (\text{C1})$$

where s_k is the entropy of particle k and $R_{d,k} = |\mathbf{x}_k - \mathbf{x}_c|$. The index k runs particles of which entropy are in the range of $s(R_d) \pm 0.5$ and $R_d < R_{200}$. We use a very strong power of the inverse of the entropy as the weight function to determine the entropy core. The outer part of the entropy profile of clusters of galaxies, typically in the range of $0.2 \leq R/R_{200} \leq 1.0$, follows $\sim (R/R_{200})^{1.1 \sim 1.2}$ (Tozzi & Norman 2001; Voit et al. 2005). Therefore, a weight which is stronger than $1/s_j^{1.1 \sim 1.2}$ is suitable in order to evaluate of the core. After intense tests, we found that the weight, $\exp(-4s_j) = 1/\exp(s_j)^4$, is suitable in

¹⁰ We prepare 15 bins which covers from 0.01 Mpc to 10 Mpc from the density center. The constant interval with the logarithmic scale is used. We calculate the entropy of each particle and add it to a bin which covers the position of the particle. We obtain the radial entropy profile of the cluster by taking the average of entropy in each bin. The averaged entropy at the given R_d is calculated by the linear interpolation of the binning values. If $R_d < 0.01$ Mpc, we use $s(R_d = 0.01 \text{ Mpc})$ as the averaged entropy at the given R_d .

order to evaluate the core radius of the radial entropy profile.

D. THE CLUMP FINDER

We adopt the subfind algorithm (Springel et al. 2001) in order to extract self-bound clumps in the Santa Barbara cluster. The procedure is as follows. First, we calculate the density of all particles within R_{200} using Eq (4). The density of gas particles is evaluated by counting the contribution of gas particles while that of DM particles is calculated by counting the contribution of DM particles. The density of each particle is evaluated by the contribution from the nearest 128 ± 8 particles. Here, we refer these nearest particles “local particles”. After the density evaluation, we sort all of particles in the descending order of the density.

We, then, identify isolate clumps following the density distribution. We repeatedly compare the densities of particles with those in the densities of their local particles from the highest to the lowest density particles and apply the following operation. Here, we focus a particle i . If the particle i is the highest density particle in its local particles, we set the particle i as the peak of an isolate clump (the core of a new clump). If the particle i is the second highest density particle or it has two higher density particles which are in the same clump, we add the particle i to the clump which includes the highest density particle. If the particle i has more than two higher density particles and the two highest density particles are in different clumps, we tag these two clumps as *the subfind clump candidates* since the particle i is at the saddle point which separate two clumps (two density peaks). Then, we merge these clumps with a single larger clump and attach particle i to this clump. The last operation is necessary in order to extract subfind clump candidates which are located at the envelop of this merged clump.

As the final step, we remove unbound particles from the subfind clump candidates iteratively. We first calculate the total energy (the self-gravitational potential and the kinematic energy where the mean velocity of each clump is set to zero) of each particle in a clump. Then if the clump includes particles of which total energy is larger than zero, we remove these particles from the clump. We do not remove more than 10% of the particles at once so that we can carry out this process stably. We continue this procedure until the clump consists only of the bound particles. We adopt clumps which contains more than 64 bound particles. We apply this procedure to all clumps and get a full catalog of subfind clumps.

E. MASS FUNCTIONS OF SUBSTRUCTURES

In this section we investigate the mass functions of substructures. The subclumps are extracted using the subfind algorithm (see §D).

Figure 24 shows mass functions of substructures. Mass functions of the runs with the same resolutions have almost identical profiles. All of mass functions asymptotically follow the power law profile with the index of ~ -1 . It is not surprising that there is no impact on substructure mass functions with different schemes, since the amount of the baryonic component is $\sim 10\%$ of the total

mass.

Mass functions of the baryonic component is shown

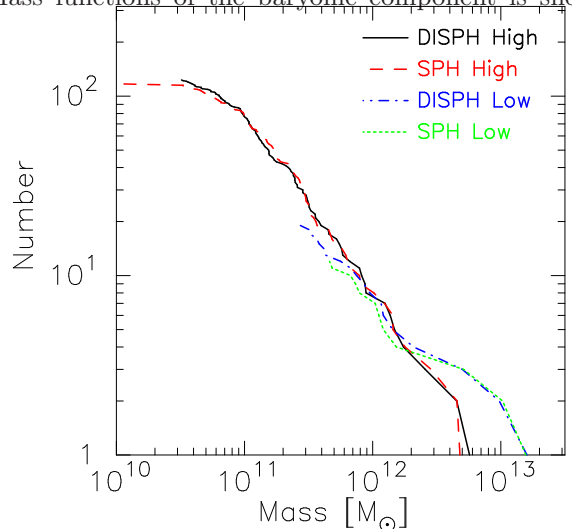


FIG. 24.— Cumulative mass functions of substructures found in the cluster with different resolutions and different schemes.

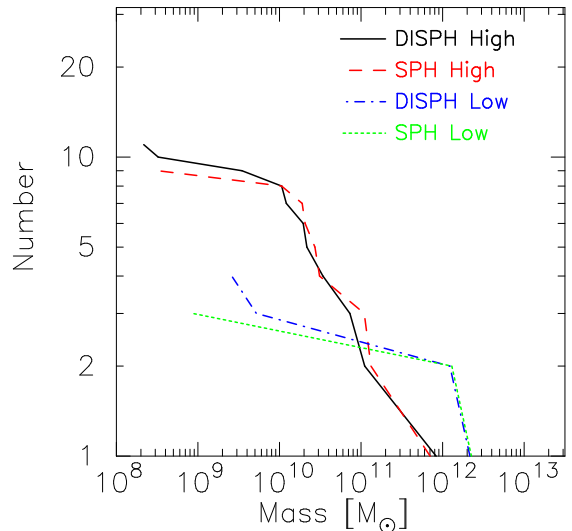


FIG. 25.— The same as figure 24, but for baryons found in substructures.

in figure 25. Not all of substructures hold the baryonic component due to the stripping. Thus, the number of baryonic substructures is very small compared to that of the total substructures. Even though the evolution of the gas clumps in the central area of the cluster is quite different for two runs, this difference is little or no effect on the mass function. This is probably because in either case that lifetime of gas clump in the central area is short.

Our mass functions do not show convergence with different mass resolutions. We have checked mass functions with mixed resolutions and found that, at least toward the high mass end, the functional form of mass functions depends on the mass resolution. Thus, the discrepancy between high-mass resolution runs and low-mass resolution runs comes from the non-linear effect induced by the smallest scale density fluctuations.

REFERENCES

- Abel, T. 2011, *MNRAS*, 413, 271
- Agertz, O., et al. 2007, *MNRAS*, 380, 963
- Almgren, A. S., Bell, J. B., Lijewski, M. J., Lukić, Z., & Van Andel, E. 2013, *ApJ*, 765, 39
- Ascasibar, Y., Yepes, G., Müller, V., & Gottlöber, S. 2003, *MNRAS*, 346, 731
- Balsara, D. S. 1995, *Journal of Computational Physics*, 121, 357
- Barnes, J., & Hut, P. 1986, *Nature*, 324, 446
- Beck, A. M., et al. 2016, *MNRAS*, 455, 2110
- Benz, W., Slattery, W. L., & Cameron, A. G. W. 1987, *Icarus*, 71, 30
- Biffi, V., & Valdarnini, R. 2015, *MNRAS*, 446, 2802
- Bryan, G. L., & Norman, M. L. 1997, *ArXiv Astrophysics e-prints:9710187*
- Bryan, G. L., Norman, M. L., Stone, J. M., Cen, R., & Ostriker, J. P. 1995, *Computer Physics Communications*, 89, 149
- Cameron, A. G. W. 1997, *Icarus*, 126, 126
- Canup, R. M. 2004, *Icarus*, 168, 433
- Canup, R. M., & Asphaug, E. 2001, *Nature*, 412, 708
- Cha, S.-H., Inutsuka, S.-I., & Nayakshin, S. 2010, *MNRAS*, 403, 1165
- Cullen, L., & Dehnen, W. 2010, *MNRAS*, 408, 669
- Dehnen, W., & Aly, H. 2012, *MNRAS*, 425, 1068
- Evvard, A. E. 1988, *MNRAS*, 235, 911
- Frenk, C. S., et al. 1999, *ApJ*, 525, 554
- Fryxell, B., et al. 2000, *ApJS*, 131, 273
- García-Senz, D., Cabezón, R. M., & Escartín, J. A. 2012, *A&A*, 538, A9
- Gingold, R. A., & Monaghan, J. J. 1977, *MNRAS*, 181, 375
- Harten, A., Engquist, B., Osher, S., & Chakravarthy, S. R. 1987, *Journal of Computational Physics*, 71, 231
- Heitmann, K., Ricker, P. M., Warren, M. S., & Habib, S. 2005, *ApJS*, 160, 28
- Hernquist, L., & Katz, N. 1989, *ApJS*, 70, 419
- Hopkins, P. F. 2013, *MNRAS*, 428, 2840
- . 2015, *MNRAS*, 450, 53
- Hosono, N., Saitoh, T. R., & Makino, J. 2013, *PASJ*, 65, 108
- . 2016a, *ArXiv e-prints:1601.05903*
- Hosono, N., Saitoh, T. R., Makino, J., Genda, H., & Ida, S. 2016b, *ArXiv e-prints:1602.00843*
- Hu, C.-Y., Naab, T., Walch, S., Moster, B. P., & Oser, L. 2014, *MNRAS*, 443, 1173
- Inutsuka, S.-I. 2002, *Journal of Computational Physics*, 179, 238
- Kawata, D., Okamoto, T., Gibson, B. K., Barnes, D. J., & Cen, R. 2013, *MNRAS*, 428, 1968
- Kravtsov, A. V., Klypin, A., & Hoffman, Y. 2002, *ApJ*, 571, 563
- Li, S. 2010, *Journal of Computational and Applied Mathematics*, 233, 3139
- Liu, X.-D., Osher, S., & Chan, T. 1994, *Journal of Computational Physics*, 115, 200
- Lucy, L. B. 1977, *AJ*, 82, 1013
- Makino, J. 1991a, *PASJ*, 43, 859
- . 1991b, *PASJ*, 43, 621
- . 2004, *PASJ*, 56, 521
- McMillan, S. L. W. 1986, in *Lecture Notes in Physics*, Berlin Springer Verlag, Vol. 267, The Use of Supercomputers in Stellar Dynamics, ed. P. Hut & S. L. W. McMillan, 156–+
- Mitchell, N. L., McCarthy, I. G., Bower, R. G., Theuns, T., & Crain, R. A. 2009, *MNRAS*, 395, 180
- Monaghan, J. J. 1997, *Journal of Computational Physics*, 136, 298
- Morris, J. P., & Monaghan, J. J. 1997, *Journal of Computational Physics*, 136, 41
- Nakajima, M., & Stevenson, D. J. 2014, *Icarus*, 233, 259
- Okamoto, T., Jenkins, A., Eke, V. R., Quilis, V., & Frenk, C. S. 2003, *MNRAS*, 345, 429
- Power, C., Read, J. I., & Hobbs, A. 2014, *MNRAS*, 440, 3243
- Price, D. J. 2008, *Journal of Computational Physics*, 227, 10040
- . 2012, *MNRAS*, 420, L33
- Read, J. I., & Hayfield, T. 2012, *MNRAS*, 422, 3037
- Read, J. I., Hayfield, T., & Agertz, O. 2010, *MNRAS*, 405, 1513
- Ritchie, B. W., & Thomas, P. A. 2001, *MNRAS*, 323, 743
- Robertson, B. E., Kravtsov, A. V., Gnedin, N. Y., Abel, T., & Rudd, D. H. 2010, *MNRAS*, 401, 2463
- Rosswog, S. 2009, *New Astron. Rev.*, 53, 78
- . 2015, *MNRAS*, 448, 3628
- Saitoh, T. R., Daisaka, H., Kokubo, E., Makino, J., Okamoto, T., Tomisaka, K., Wada, K., & Yoshida, N. 2008, *PASJ*, 60, 667
- . 2009, *PASJ*, 61, 481
- Saitoh, T. R., & Makino, J. 2009, *ApJL*, 697, L99
- . 2010, *PASJ*, 62, 301
- . 2012, *New Astronomy*, 17, 76
- . 2013, *ApJ*, 768, 44
- Sembolini, F., et al. 2016, *MNRAS*, 457, 4063
- Sijacki, D., Vogelsberger, M., Kereš, D., Springel, V., & Hernquist, L. 2012, *MNRAS*, 424, 2999
- Springel, V. 2005, *MNRAS*, 364, 1105
- . 2010, *MNRAS*, 401, 791
- Springel, V., & Hernquist, L. 2002, *MNRAS*, 333, 649
- Springel, V., White, S. D. M., Tormen, G., & Kauffmann, G. 2001, *MNRAS*, 328, 726
- Steinmetz, M., & Mueller, E. 1993, *A&A*, 268, 391
- Stone, J. M., & Norman, M. L. 1992, *ApJS*, 80, 753
- Tanikawa, A., Yoshikawa, K., Nitadori, K., & Okamoto, T. 2013, *New Astronomy*, 19, 74
- Tasker, E. J., Brunino, R., Mitchell, N. L., Michielsen, D., Hopton, S., Pearce, F. R., Bryan, G. L., & Theuns, T. 2008, *MNRAS*, 390, 1267
- Teyssier, R. 2002, *A&A*, 385, 337
- Tozzi, P., & Norman, C. 2001, *ApJ*, 546, 63
- Vazza, F. 2011, *MNRAS*, 410, 461
- Voit, G. M., Kay, S. T., & Bryan, G. L. 2005, *MNRAS*, 364, 909
- von Hoerner, S. 1960, *ZAp*, 50, 184
- . 1963, *ZAp*, 57, 47
- Wadsley, J. W., Veeravalli, G., & Couchman, H. M. P. 2008, *MNRAS*, 387, 427
- Wendland, H. 1995, *Advances in computational Mathematics*, 4, 389
- Yabe, T., & Aoki, T. 1991, *Computer Physics Communications*, 66, 219
- Yamamoto, S., Saitoh, T. R., & Makino, J. 2015, *PASJ*, 67, 37